UNIVERSITÀ DEGLI STUDI DI PADOVA
DIPARTIMENTO DI SCIENZE CHIMICHE

CORSO DI LAUREA MAGISTRALE IN CHIMICA

TESI DI LAUREA MAGISTRALE

Study on the Ultrafast Dynamics of Solid-state Semiconductor Nanocrystals (QDs) for Quantum Technologies Applications

Relatore: Prof.ssa Elisabetta Collini
Controrelatore: Prof. Mauro Sambi

Laureanda: Matilde Doardo

ANNO ACCADEMICO 2023/2024

II

Table of Contents

Abstract - English

The recent development of quantum technologies requires the urgent design, preparation and characterization of materials with engineerable quantum-coherent behaviours. Quantum dots (QDs), which are semiconductor nanocrystals with exceptional optical and photophysical properties, are particularly promising candidates for this application.

However, the increasing complexity of the materials and their functionalities requires the development of equally complex techniques to probe their response. In view of this need, ultrafast bidimensional spectroscopy (2DES) emerged as a powerful and versatile technique in the investigation of materials to be employed in recently proposed quantum technology applications. In particular, the recently developed action-based approach (A-2DES) promises to be particularly suitable for unravelling the intricacies of quantum phenomena in real devices, especially in the context of emerging quantum technologies. However, only a few works on this approach are currently available in the literature. The experimental layout of the technique is not yet optimized, and the effective meaning of the collected signal is the object of debate in the community.

In this thesis, we applied A-2DES to the study of a QD-based optoelectronic device to demonstrate the capability of this technique to probe the ultrafast behaviour of real devices.

Abstract - Italiano

Il recente sviluppo delle tecnologie quantistiche richiede urgentemente la progettazione, preparazione e caratterizzazione di materiali con comportamenti quantistici manipolabili. I quantum dots (QDs), ovvero nanocristalli semiconduttori con eccezionali proprietà ottiche e fotofisiche, sono dei candidati particolarmente promettenti per questa applicazione. Tuttavia, l'aumentare della complessità dei materiali e delle loro funzionalità richiede lo sviluppo di tecniche altrettanto complesse per poterli caratterizzare. In virtù di questa esigenza, la spettroscopia elettronica bidimensionale (2DES) si è dimostrata una tecnica potente e versatile per quanto riguarda l'indagine di materiali destinati alle applicazioni delle tecnologie quantistiche recentemente proposte. In particolare, l'approccio "action-based" (A-2DES) recentemente sviluppato, sembra essere particolarmente adatto per svelare le complessità dei fenomeni quantistici nei dispositivi reali. Tuttavia, attualmente, in letteratura sono disponibili solo pochi lavori che trattano questo approccio. La configurazione sperimentale della tecnica non è ancora ottimizzata e il significato effettivo del segnale raccolto è oggetto di dibattito nella comunità scientifica.

In questa tesi, abbiamo applicato l'A-2DES allo studio di un dispositivo optoelettronico basato su QDs per dimostrare la capacità di questa tecnica di poter esplorare il comportamento ultraveloce di dispositivi reali.

List of Abbreviations

2DES	Two-dimensional Electronic Spectroscopy
A-2DES	Action-based Two-dimensional Electronic Spectroscopy
AOM	Acousto-optic Modulator
AOPDF	Acousto-optic Programmable Dispersive Filter
BBO	Beta Barium Borate
EFA	Envelope Function Approximation
EMA	Effective Mass Approximation
GDD	Group Delay Dispersion
LCAO	Linear Combination of Atomic Orbitals
NOPA	Non-collinear Optical Parametric Amplifier
NR	Non-rephasing
PC-2DES	Photocurrent-detected Two-dimensional Electronic Spectroscopy
PIS	Particle in a Sphere
QD	Quantum Dot
R	Rephasing
RF	Radio Frequency
TEM	Transmission Electronic Microscopy
pDT	1,3 propanedithiol

Introduction

Spectroscopy, a milestone in the study of matter and its interactions with light, represents one of the most powerful tools to investigate the fundamental properties of different natural and artificial materials. As the boundaries of scientific research extend further towards increasingly complex systems, the development of advanced techniques capable of studying and characterizing their features becomes paramount.

In the context of optical spectroscopy, two-dimensional electronic spectroscopy (2DES) stands as a pivotal technique with immense significance in unravelling the complexities of molecular and electronic interactions. Its unique capability to explore ultrafast processes on femtosecond timescales offers an insightful perspective into the intricate relations between chromophores within congested molecular systems [1-3].
By capturing electronic coherences and correlations in both time and frequency domains, 2DES unveils a comprehensive picture of molecular dynamics, offering unprecedented insights into phenomena that can significantly affect many fields, from chemistry and physics to materials science [4].

In recent times, a newly implemented and very promising approach, named action-based 2DES (A-2DES), has emerged. By probing coherent dynamics induced through the interaction with four collinear ultrashort laser pulses, this method relies on measuring an incoherent signal proportional to the excited-state population, such as fluorescence or photocurrent. This capability enables the exploration of the dynamics of systems under in *operando* conditions and, therefore, is particularly suitable to characterize quantum devices. [4,5]
Therefore, action-based 2DES promises to open up a new dimension in our capacity to not only observe quantum processes but also harness their potential for transformative applications in the field of quantum technologies. This real-time feedback mechanism allows for the precise characterization of quantum states and facilitates the exploration of quantum coherences and entanglement.

In the pursuit of quantum-based technologies such as quantum computing, communication and sensing, understanding and controlling quantum states is crucial. Action-based approaches of 2DES enable the probing of quantum materials and devices with unprecedented accuracy, offering critical insights into the behavior of quantum states under varying conditions.

Despite the growing interest in A-2DES, a notable research gap exists in fully harnessing its potential for quantum-based technologies.

This thesis has the objective of providing a contribution to fill this gap. Specifically, we performed photocurrent-detected 2DES experiments on a QDs-based optoelectronic device. The aim was not only to contribute to the characterization and understanding of quantum phenomena in this specific device but also to optimize the practical implementation of this innovative approach and find new technical solutions to optimize its development.

The following chapters will delve into:
- The theoretical formalisms necessary to the understanding of the technique (Chapter 1).
- A comparison between the conventional coherence-based approach vs. the action-based approach for 2DES experiments (Chapter 2).
- A brief introduction to the electronic and optical properties of semiconductor quantum dots (QDs), the systems object of this thesis (Chapter 3).
- A description of the experimental methods employed to perform the experiments (Chapter 4).
- A discussion of the preliminary results achieved by applying the photocurrent-detected 2DES technique to a QDs-based optoelectronic device (Chapter 5).

Chapter 1
Theoretical Background to Nonlinear Spectroscopies

Before venturing into the field of nonlinear optical spectroscopy, it is necessary to revise a few fundamental concepts and formalisms at its basis. In this chapter, a brief overview of such topics as originally formalized by Mukamel [6] is presented, starting from the macroscopic description of the light-matter interaction in terms of the macroscopic polarization $\boldsymbol{P}$, up to the microscopic approach in terms of the *time-dependent perturbation theory* and of the *response function formalism.*

1.1 Light-matter Interaction

All kinds of spectroscopies, being of the magnetic or the optical type, revolve around the same basic concept: they all study matter through its interaction with light (i.e. electromagnetic) fields.

Like in all problems of this nature, it is necessary to derive the Hamiltonian for such interaction, which in the most general case would be of the form [7]:

$$H = H_M + H_L + H_{LM} \qquad (1.1)$$

This Hamiltonian is defined as the sum of three terms, accounting for matter, light, and their interaction, respectively. A pure quantum mechanical treatment, in which both light and matter are treated quantum mechanically, would be highly demanding since it would require simultaneously solving the coupled equation of motion for both light and matter variables. In order to avoid such complex calculations, we can make use of the well-known *semiclassical*

approximation, which allows us to drastically simplify the problem. According to this approximation, only matter is treated from the quantum mechanical point of view, whereas light is treated classically as a wave. Therefore, light is considered as a perturbation that acts on the system, inducing a charge redistribution in the medium, but that is not affected by matter. In this case, the Hamiltonian term relative to light can be discarded and the resulting Hamiltonian of the system will assume this form:

$$H \approx H_M + H_{LM}. \tag{1.2}$$

From a physical point of view, when considering a charge redistribution induced by a field in a medium, it is appropriate to describe this phenomenon in terms of the polarization field $\boldsymbol{P}$. This macroscopic quantity accounts for the response of the medium when exposed to an electric field and quantifies the charge redistribution induced within the medium. Polarization is a fundamental quantity in optical spectroscopies because the signal is proportional to it.

Within the semiclassical approximation, the dynamics of the system is calculated by solving the coupled equations for the electric field $\boldsymbol{E}(\boldsymbol{r})$ and for the polarization $\boldsymbol{P}(\boldsymbol{r})$. The expression for the polarization results from the Maxwell-Liouville equations [6]:

$$\nabla \times \nabla \times \boldsymbol{E}(\boldsymbol{r},t) + \frac{1}{c^2}\frac{\partial^2}{\partial t^2}\boldsymbol{E}(\boldsymbol{r},t) = -\frac{4\pi}{c^2}\frac{\partial^2 \boldsymbol{P}(\boldsymbol{r},t)}{\partial t^2} \tag{1.3}$$

For a weak electric field, the polarization depends linearly on the strength of the electric field. However, in dealing with ultrafast pulses and intense electric fields, nonlinear effects become non-negligible and therefore the polarization has to be described more in general as a power expansion of the electric field:

$$\boldsymbol{P} = \varepsilon_0 \left[\chi^{(1)} \cdot \boldsymbol{E} + \chi^{(2)} : \boldsymbol{E} \cdot \boldsymbol{E} + \chi^{(3)} \vdots \boldsymbol{E} \cdot \boldsymbol{E} \cdot \boldsymbol{E} + \cdots \right] \tag{1.4}$$

where:

- ε_0 is the permittivity of vacuum,
- $\chi^{(n)}$ is the nth order susceptibility, a tensorial quantity. For n=1, the linear term is retrieved,
- $\boldsymbol{E}$ is the electric field.

At this point, we can separate $\boldsymbol{P}$ into its linear and nonlinear contributions, i.e.:

$$\boldsymbol{P}(\boldsymbol{r},t) \equiv \boldsymbol{P}^{(1)}(\boldsymbol{r},t) + \boldsymbol{P}^{NL}(\boldsymbol{r},t), \tag{1.5}$$

where:

- $\boldsymbol{P}^{(1)}$ is linear in $\boldsymbol{E}$,
- $\boldsymbol{P}^{NL}$ accounts for all nonlinear contributions.

In the following Sections (1.4, 1.5) we will show how the macroscopic polarization in nonlinear spectroscopies is related to the *response function S^{(3)}* but before we need to dive deeper into the formalisms of quantum mechanics.

1.2 Time Evolution of the Wave Function

A quantum system is described in terms of its wave function $|\psi(t)\rangle$, whose time evolution can be calculated by solving the time-dependent Schrödinger equation:

$$\frac{\partial|\psi(t)\rangle}{\partial t} = -\frac{i}{\hbar}H|\psi(t)\rangle, \tag{1.6}$$

where:

- H represents the Hamiltonian of the system,
- $\hbar$ is the reduced Planck's constant.

The most common approach to solve this equation in the context of spectroscopical methods is by far the *time-dependent perturbation theory* through the introduction of the *time evolution operator U*, defined as:

$$|\psi(t)\rangle \equiv U(t, t_0)|\psi(t_0)\rangle, \tag{1.7}$$

which acts as a propagator on the wavefunction to the right, by propagating the system from the starting time t_0 to the observation time t.

For a time-independent Hamiltonian, we easily obtain the following expression for the time evolution operator:

$$U(t, t_0) = e^{-\frac{i}{\hbar}H \cdot (t - t_0)}. \tag{1.8}$$

1.2.1 Properties of the Time Evolution Operator

In this section we will introduce some fundamental properties of the time evolution operator, in order to better understand its action on the wavefunction [7].

We start this description by stating that the propagator cannot depend on the state of the system. This condition is, in fact, necessary to retain the normalization of the system.

If

$$\psi(t_0)\rangle = a_1|\varphi_1(t_0)\rangle + a_2|\varphi_2(t_0)\rangle, \tag{1.9}$$

Then:

$$|\psi(t)\rangle = U(t_0, t)|\psi(t_0)\rangle \tag{1.10}$$

$$|\psi(t)\rangle = U(t_0, t)a_1|\varphi_1(t_0)\rangle + U(t_0, t)a_2|\varphi_2(t_0)\rangle \tag{1.11}$$

$$|\psi(t)\rangle = a_1(t)|\varphi_1(t_0)\rangle + a_2(t)|\varphi_2(t_0)\rangle. \tag{1.12}$$

Equation 1.12 is valid due to the application of the principles of *linearity* and *superposition* in quantum mechanical systems.

We will now define four important properties of this time evolution operator U, which will be useful in later calculations:

1. Unity: this property must be satisfied to conserve the probability density
$$P = \langle \psi(t)|\psi(t)\rangle = \langle \psi(t_0)|U^\dagger U|\psi(t_0)\rangle$$

2. Time continuity:
$$U(t,t) = 1$$

3. Composition property:
$$U(t_2,t_0) = U(t_2,t_1)U(t_1,t_0)$$

4. Time-reversal property:
$$U(t,t_0)U(t_0,t) = 1$$
$$\therefore U^{-1}(t,t_0) = U(t_0,t).$$

1.2.2 Propagation of the Wavefunction in the Interaction Picture

In order to study the dynamics of the system over time, we must solve the time-dependent Schrödinger equation, but it is worth noting that substituting Equation1.7 into the time-dependent wavefunction is equivalent to solving the equation of motion for the time evolution operator. In fact:

$$\frac{d}{dt}|\psi(t)\rangle = -\frac{i}{\hbar}H|\psi(t)\rangle \tag{1.13}$$

$$\frac{d}{dt}U(t,t_0)|\psi(t_0)\rangle = -\frac{i}{\hbar}H\cdot U(t,t_0)|\psi(t_0)\rangle \tag{1.14}$$

$$\frac{d}{dt}U(t,t_0) = -\frac{i}{\hbar}H\cdot U(t,t_0). \tag{1.15}$$

To evaluate the behaviour of the time evolution operator over time, it is convenient to move from the Schrödinger picture[1] to the so-called "Interaction picture" or "Dirac representation". In the *interaction picture* both the state vectors and the operators bring the time dependence [6].

This representation is particularly convenient when the total Hamiltonian of the system can be factorized into two different contributions:

$$H(t) = H_0(t) + H'(t) \tag{1.16}$$

where $H_0(t)$ is generally well known and defined (i.e. analytical solutions are available), and the second one $H'(t)$ accounts for a *weak* time dependency that will be treated perturbatively. We shall now introduce the time evolution operator with respect to H_0, U_0, which satisfies the equation [7]:

$$\frac{\partial}{\partial t} U_0(t, t_0) = -\frac{i}{\hbar} H_0(t) U_0(t, t_0) \tag{1.17}$$

whose solution is:

$$U_0(t, t_0) = \tag{1.18}$$

$$= exp_+ \left[-\frac{i}{\hbar} \int_{t_0}^{t} d\tau \, H_0(\tau) \right]$$

$$\equiv 1 + \sum_{n=1}^{\infty} \left(\frac{-i}{\hbar} \right)^n \int_{t_0}^{t} d\tau_n \int_{t_0}^{\tau} d\tau_n \dots \int_{t_0}^{t} d\tau_1 H(\tau_n) H(\tau_{n-1}) \dots H(\tau_1)$$

with *exp₊* being a positive time-ordered exponential [7].

---

[1] In the frame of the Schrödinger picture, the time dependence is fully contained in the state vectors, while the operators are time independent.

This expression is achieved by performing an iterative substitution of U into itself and gives information about the evolution of a quantum system over a given time interval. The time ordering of this exponential is:

$$t_0 \to \tau_1 \to \tau_2 \to \tau_3 \dots \tau_n \to t.$$

We define the wavefunction in the interaction picture $|\psi_I(t)\rangle$ as follows:

$$|\psi_s(t)\rangle \equiv U_0(t, t_0)|\psi_I(t)\rangle, \tag{1.19}$$

Where $|\psi_s(t)\rangle$ is the wavefunction defined in the Schrödinger picture.

When introducing Equation 1.19 into the Schrödinger equation:

$$-\frac{i}{\hbar} H|\psi(t)\rangle = \frac{d}{dt}|\psi(t)\rangle \tag{1.20}$$

$$-\frac{i}{\hbar} H(t) \cdot U_0(t, t_0)|\psi_I(t)\rangle = \frac{d}{dt}(U_0(t, t_0)|\psi_I(t)\rangle) \tag{1.21}$$

$$= \left(\frac{d}{dt}(U_0(t, t_0))\right) \cdot |\psi_I(t)\rangle + U_0(t, t_0)\left(\frac{d}{dt}|\psi_I(t)\rangle\right) \tag{1.22}$$

$$= -\frac{i}{\hbar} H_0 \cdot U_0(t, t_0) \cdot |\psi_I(t)\rangle + U_0(t, t_0) \cdot \left(\frac{d}{dt}|\psi_I(t)\rangle\right) \tag{1.23}$$

Now, since $H'(t) = H(t) - H_0$,

$$-\frac{i}{\hbar} H'(t) \cdot U_0(t, t_0)|\psi_I(t)\rangle = U_0(t, t_0) \cdot \left(\frac{d}{dt}|\psi_I(t)\rangle\right) \tag{1.24}$$

Or

$$-\frac{i}{\hbar}U_0^\dagger(t,t_0)H'(t)\cdot U_0(t,t_0)|\psi_I(t)\rangle = \frac{d}{dt}|\psi_I(t)\rangle \tag{1.25}$$

$$\implies \frac{d}{dt}|\psi_I(t)\rangle = -\frac{i}{\hbar}H_I'(t)|\psi_I(t)\rangle \tag{1.26}$$

Where the weak perturbation $H_I'(t)$ in the interaction picture is:

$$H_I'(t) = U_0^\dagger(t,t_0)H'(t)U_0(t,t_0) \tag{1.27}$$

or

$$H_I'(t) = e^{\frac{i}{\hbar}H_0\cdot(t-t_0)}H'(t)e^{-\frac{i}{\hbar}H_0\cdot(t-t_0)}. \tag{1.28}$$

Equation 1.26 is formally equivalent to Equation 1.13 and can be solved by performing an iterative substitution:

$$\begin{aligned}|\psi_I(t)\rangle &= |\psi_I(t_0)\rangle \\ &+ \sum_{n=1}^{\infty}\left(-\frac{i}{\hbar}\right)^n\int_{t_0}^{t}d\tau_n\int_{t_0}^{\tau_n}d\tau_{n-1}\ldots\int_{t_0}^{\tau_2}d\tau_1 H_I'(\tau_n)H_I'(\tau_{n-1})\ldots H_I'(\tau_1)|\psi_I(t_0)\rangle\end{aligned} \tag{1.29}$$

It is important to observe that this is an expansion in powers of the weak perturbation $H'(t)$, and not of the full time-dependent Hamiltonian.

The physical intuition behind this expression is the following (Figure 1.1): the system is in an equilibrium condition until time τ_1 (i.e. $U(\tau_1,t_0)$). At time τ_1 it interacts with the perturbation $H'(\tau_1)$. After this interaction, it will again freely propagate until time τ_2, when it interacts with the perturbation $H'(\tau_2)$, and so on. This interpretation can be visualized by means of a single-sided Feynman diagram, which graphically represents the perturbative expansion of the wavefunction (see Section 1.5.2 for a more explicit explanation of Feynman diagrams).
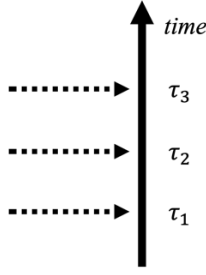
Figure 1.1: *Diagrammatic representation of the perturbative expansion of the wavefunction. The vertical arrow represents the time evolution of the system, whereas the dotted arrows depict the interaction with the perturbation H' at times τ_n.*

1.3 Density operator

We will now introduce the *density operator* and its matrix representation, another fundamental tool that is particularly useful in the description of quantum systems, especially when the time-dependency and the presence of *mixed states[2]* must be taken into account. From the physical point of view, the density operator is analogous to the wavefunction, but supplies significant practical advantages, as shown below.

The density matrix is defined as the outer product of the wavefunction with its complex conjugate [7]:

$$\rho(t) \equiv |\psi(t)\rangle\langle\psi(t)| \tag{1.30}$$

The mathematical advantage in performing calculations with the use of the density operator is evident when the expectation values of operators must be evaluated. In fact, if we expand the wavefunction of a system into its basis set we obtain:

$$|\psi(t)\rangle = \sum_n c_n(t)|n\rangle, \tag{1.31}$$

---

[2] Mixed states are statistical mixtures which cannot be described in terms of a single wavefunction. Therefore, the information about the quantum system can be gained only by performing statistical averages.

where c_n are the complex expansion coefficients.

We now recall that the expectation value of an operator is defined as:

$$\langle A(t) \rangle = \sum_{n,m} c_n(t)c_m^*(t)\langle m|A|n \rangle. \tag{1.32}$$

And from the previous definition of the density operator (Equation 1.30), one obtains:

$$\rho(t) = \sum_{n,m} c_n(t)c_m^*(t)\,|n\rangle\langle m| \tag{1.33}$$

$$\equiv \sum_{n,m} \rho_{nm}(t)\,|n\rangle\langle m| \tag{1.34}$$

Where $\rho_{nm}(t)$ are the elements of the density matrix, defined by the time-evolving expansion coefficients.

Equation 1.32 now becomes:

$$\langle A(t) \rangle = \sum_{n,m} A_{mn}\rho_{nm}(t) \tag{1.35}$$

$$= Tr[A\rho(t)] \tag{1.36}$$

Where $Tr[...]$ refers to tracing (i.e. summing) over the diagonal elements of the matrix. This reduces the evaluation of the expectation value of an operator to tracing over a product of matrices, instead of performing an integration.

1.3.1 Properties of the density operator

In this section some important properties and definitions of the density operator are presented, which will be useful for the following calculations.

From the definition above, it follows that:

1. The density operator is Hermitian, since $\rho_{nm} = \rho_{mn}^*$

2. Probability must be normalized, which implies that $Tr(\rho) = 1$

3. The degree of pureness of a quantum state can be evaluated from the calculation of the trace of the density operator. In fact:

$$Tr(\rho^2) = \begin{cases} = 1 \; for \; a \; pure \; state \\ < 1 \; for \; a \; mixed \; state \end{cases}$$

Since in this work terms "populations" and "coherences" will be recurrent, it is necessary to explain what this nomenclature stands for.

The elements of the density matrix can be divided into two categories:

- The diagonal elements $(n = m)$, also known as "populations", which give the probability of occupying a quantum state:

$$\rho_{nn} = c_n c_n^* = p_n \geq 0,$$

- The off-diagonal elements $(n \neq m)$, also known as "coherences", since they account for the coherent oscillatory behaviour of a coherent superposition of states of the system. Coherences are complex quantities and bring a time-dependent phase factor:

$$\rho_{nm} = c_n(t)c_m^*(t) = c_n c_m^* e^{-i\omega_{mn}t}.$$

We previously mentioned the importance of the density matrix when dealing with mixed states. In fact, if the probability p_k of occupying a quantum state $|\psi_k\rangle$ is defined, the expression for $\rho(t)$ becomes:

$$\rho(t) \equiv \sum_k p_k |\psi_k(t)\rangle\langle\psi_k(t)| \tag{1.37}$$

And the evaluation of the expectation value for the generic operator A:

$$\langle A(t)\rangle = \sum_k p_k \langle\psi_k(t)|A|\psi_k(t)\rangle \tag{1.38}$$

$$\langle A(t)\rangle = Tr[A\rho(t)]. \tag{1.39}$$

This is the expression obtained in Equation 1.36 for a pure state.

1.3.2 Time evolution of the density operator

We will start the description of the time evolution of the density operator by deriving its equation of motion. For the sake of simplicity, we will only consider the case of a pure state, but the treatment can be easily generalized also for a mixed state.

$$\frac{\partial \rho}{\partial t} = \left(\frac{\partial}{\partial t}|\psi(t)\rangle\right)\langle\psi(t)| + |\psi(t)\rangle\left(\frac{\partial}{\partial t}|\psi(t)\rangle\right) \tag{1.40}$$

Using the Schrödinger equation and its Hermitian conjugate, we get:

$$\frac{\partial \rho}{\partial t} = -\frac{i}{\hbar}H|\psi\rangle\langle\psi| + \frac{i}{\hbar}|\psi\rangle\langle\psi|H \tag{1.41}$$

$$= -\frac{i}{\hbar}(H\rho - \rho H) \tag{1.42}$$

Or

$$\frac{\partial \rho}{\partial t} = -\frac{i}{\hbar}[H, \rho], \tag{1.43}$$

Known as the Liouville-Von Neumann equation, whose solution is the following:

$$\rho(t) = U(t, t_0)\rho(t_0)U^\dagger(t, t_0). \tag{1.44}$$

If we define the density matrix in the interaction picture as

$$\rho(t) \equiv |\psi(t)\rangle\langle\psi(t)| = U_0(t, t_0) \cdot |\psi_I(t)\rangle\langle\psi_I(t)| \cdot U_0^\dagger(t, t_0) \tag{1.45}$$

Equation 1.44 still holds, and we get an equivalent expression for the Liouville-Von Neumann equation in the interaction picture, whose power expansion is:

$$\rho_I(t) =$$
$$= \rho_I(t_0)$$
$$+ \sum_{n=1}^{\infty} \left(-\frac{i}{\hbar}\right)^n \int_{t_0}^{t} d\tau_n \int_{t_0}^{\tau_n} d\tau_{n-1} \dots \int_{t_0}^{\tau_2} d\tau_1 \left[H_I'(\tau_n), [H_I'(\tau_{n-1}), \dots [H_I'(\tau_1), \rho_I(t_0)] \dots]] \right. \qquad (1.46)$$

In this expression each iterative substitution reflects an interaction between light and matter, meaning that an nth order expansion term will be proportional to the observed polarization in an nth order nonlinear spectroscopy [7].

In fact, if we specify the perturbation as

$$H'(t) = -E(t) \cdot \mu, \qquad (1.47)$$

The nth order density matrix is given by [6]:

$$\rho^n(t) = \left(-\frac{i}{\hbar}\right)^n \int_{-\infty}^{t} d\tau_n \int_{-\infty}^{\tau_n} d\tau_{n-1} \dots \int_{-\infty}^{\tau_2} d\tau_1 E(\tau_n) E(\tau_{n-1}) \cdot \dots$$
$$\cdot E(\tau_1) \cdot U_0(t, t_0)$$
$$\cdot [\mu_I(\tau_n), [\mu_I(\tau_{n-1}), \dots [\mu_I(\tau_1), \rho(-\infty)] \dots]] \cdot U_0^{\dagger}(t, t_0) \qquad (1.48)$$

Where the dipole operator in the interaction picture is defined as:

$$\mu_I(t) = U_0^{\dagger}(t, t_0) \mu U_0(t, t_0) \qquad (1.49)$$

1.4 Response Function Formalism

In the previous sections we already stressed the importance of optical polarization for the interpretation of any spectroscopic measurement. We will now introduce a general formalism, known as Response Function Theory, to describe the observable of a spectroscopic experiment.

In particular, we will focus on how the system is driven out of the thermal equilibrium by the presence of a weak (i.e. perturbative) external stimulus.

Since the stochastic nature of the sample must be considered, we will define the macroscopic polarization in terms of the density operator, which naturally accounts for the presence of statistical ensembles. In this case, the macroscopic polarization can be defined as:

$$P(t) = Tr[\boldsymbol{\mu}\boldsymbol{\rho}(t)] \equiv \langle \boldsymbol{\mu}\boldsymbol{\rho}(t) \rangle, \tag{1.50}$$

Where $\langle ... \rangle$ indicates the expectation value.

Analogously, discarding the vectorial nature of these quantities, we obtain the nth order polarization:

$$P^{(n)}(t) = \langle \mu \rho^{(n)}(t) \rangle. \tag{1.51}$$

By substituting Equation 1.48 into Equation 1.51 we get:

$$P^{(n)}(t) = \left(-\frac{i}{\hbar}\right)^n \int_0^\infty dt_n \int_0^\infty dt_{n-1} \dots \int_0^\infty dt_1 E(t - t_n) E(t - t_n - t_{n-1}) \cdot \dots$$
$$\cdot E(t - t_n - t_{n-1} - \dots - t_1)$$
$$\cdot \langle \mu(t_n + t_{n-1} + \dots t_1)[\mu(t_{n-1} + \dots + t_1), \dots [\mu(0), \rho(-\infty)] \dots] \rangle \tag{1.52}$$

Where the new set of time variables is (Figure 1.2):

$$\tau_1 = 0$$
$$t_1 = \tau_2 - \tau_1$$
$$t_2 = \tau_3 - \tau_2$$
$$\vdots$$
$$t_n = t - \tau_n$$

With $\tau_1 = 0$, arbitrarily chosen.
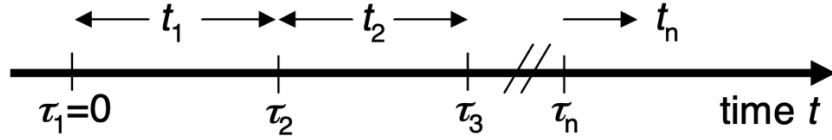
Figure 1.2: *Time ordering of the n*[th]*-order polarization. The time variables t_n denote time intervals, whereas the time variables τ_n denote absolute time points.*

The expression can be further simplified into:

$$P^{(n)}(t) = \int_0^\infty dt_n \int_0^\infty dt_{n-1} \dots \int_0^\infty dt_1 \, E(t - t_n) E(t - t_n - t_{n-1}) \cdot \dots$$
$$\cdot E(t - t_n - \dots - t_1) \cdot S(t_n, t_{n-1}, \dots, t_1), \tag{1.53}$$

Where we have finally defined the *response function S* (defined only for positive time delays t_n), as:

$$S^{(n)}(t_n, \dots t_1) = \left(-\frac{i}{\hbar}\right)^n \langle \mu(t_n + \dots t_1)[\mu(t_{n-1} + \dots$$
$$+ t_1), \dots [\mu(0), \rho(-\infty)] \dots]\rangle \tag{1.54}$$

1.5 Third Order Response Function and Diagrammatic Techniques

The third order term of the response function is of particular interest for nonlinear spectroscopies as it is the lowest order allowing for the investigation of excited states properties.

1.5.1 Third order response function in 2DES

In ultrafast bidimensional optical spectroscopies the experimentally measured signal is proportional to the third order polarization:

18

$$E_{signal} \propto iP^{(3)}(t), \tag{1.55}$$

which can be expressed in terms of the electric field and of the third order response function S^3 as:

$$P^{(3)}(t) = \int_0^\infty dt_3 \int_0^\infty dt_2 \int_0^\infty dt_1 E(t - t_3)E(t - t_3 - t_2)E(t - t_3 - t_2 - t_1)S^3(t_3, t_2, t_1) \tag{1.56}$$

$$S^{(3)}(t_3, t_2, t_1) = \left(-\frac{i}{\hbar}\right)^3 \sum_{\alpha=1}^4 [R_\alpha(t_3, t_2, t_1) - R_\alpha^*(t_3, t_2, t_1)] \tag{1.57}$$

Where the terms R_α and R_α^* are called Liouville pathways. The third order response function $S^{(3)}(t_3, t_2, t_1)$ contains $2^3 = 8$ different pathways, which are expressed as traces of the product of matrices:

$$R_1(t_3, t_2, t_1) = Tr[\hat{\mu}_I(t_1 + t_2 + t_3)\hat{\mu}_I(t_1 + t_2)\hat{\mu}_I(t_1)\hat{\mu}(0)\hat{\rho}_{eq}]$$

$$R_1^*(t_3, t_2, t_1) = Tr[\hat{\mu}_I(t_1 + t_2 + t_3)\hat{\rho}_{eq}\hat{\mu}(0)\hat{\mu}_I(t_1)\hat{\mu}_I(t_1 + t_2)]$$

$$R_2(t_3, t_2, t_1) = Tr[\hat{\mu}_I(t_1 + t_2 + t_3)\hat{\mu}_I(t_1)\hat{\rho}_{eq}\hat{\mu}(0)\hat{\mu}_I(t_1 + t_2)]$$

$$R_2^*(t_3, t_2, t_1) = Tr[\hat{\mu}_I(t_1 + t_2 + t_3)\hat{\mu}_I(t_1 + t_2)\hat{\mu}(0)\hat{\rho}_{eq}\hat{\mu}_I(t_1)] \tag{1.58}$$

$$R_3(t_3, t_2, t_1) = Tr[\hat{\mu}_I(t_1 + t_2 + t_3)\hat{\mu}_I(t_1 + t_2)\hat{\rho}_{eq}\hat{\mu}(0)\hat{\mu}_I(t_1)]$$

$$R_3^*(t_3, t_2, t_1) = Tr[\hat{\mu}_I(t_1 + t_2 + t_3)\hat{\mu}_I(t_1)\hat{\mu}(0)\hat{\rho}_{eq}\hat{\mu}_I(t_1 + t_2)]$$

$$R_4(t_3, t_2, t_1) = Tr[\hat{\mu}_I(t_1 + t_2 + t_3)\hat{\mu}(0)\hat{\rho}_{eq}\hat{\mu}_I(t_1)\hat{\mu}_I(t_1 + t_2)]$$

$$R_4^*(t_3, t_2, t_1) = Tr[\hat{\mu}_I(t_1 + t_2 + t_3)\hat{\mu}_I(t_1 + t_2)\hat{\mu}_I(t_1)\hat{\rho}_{eq}\hat{\mu}(0)]$$

Each Liouville pathway accounts for a different light-matter interaction sequence and can be more easily visualized by double-sided *Feynman diagrams*, as we will see in the following section.

It is of fundamental importance to note that spectroscopic techniques that employ *coherently emitted* electric fields are defined as "coherence-based" spectroscopies, since they measure an electric field that is originated from a coherence.

1.5.2 Diagrammatic Techniques

Equations 1.55-1.58 can be employed to formally describe nonlinear effects in the system of interest. However, they have a complex mathematical form, mainly resulting from the development of nested commutators like in Equation 1.54, which often challenges an easy interpretation of the molecular origin of the nonlinear signal [7]. In order to simplify the interpretation of the molecular response, we can make use of diagrammatic techniques, which give a visual and immediate representation of the interaction between light and the system under study, evaluated over time. Many kinds of diagrams have been proposed but here the most known *double-sided Feynman diagrams* will be considered (Figure 1.4).
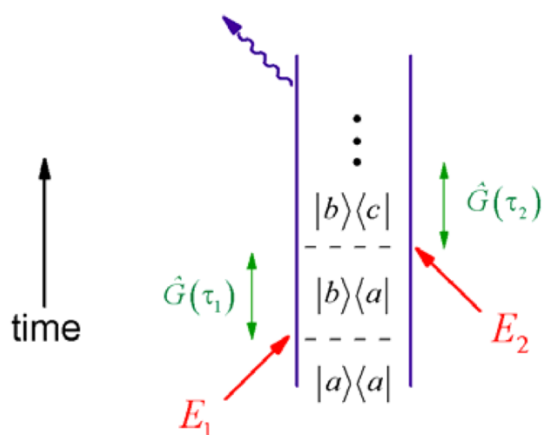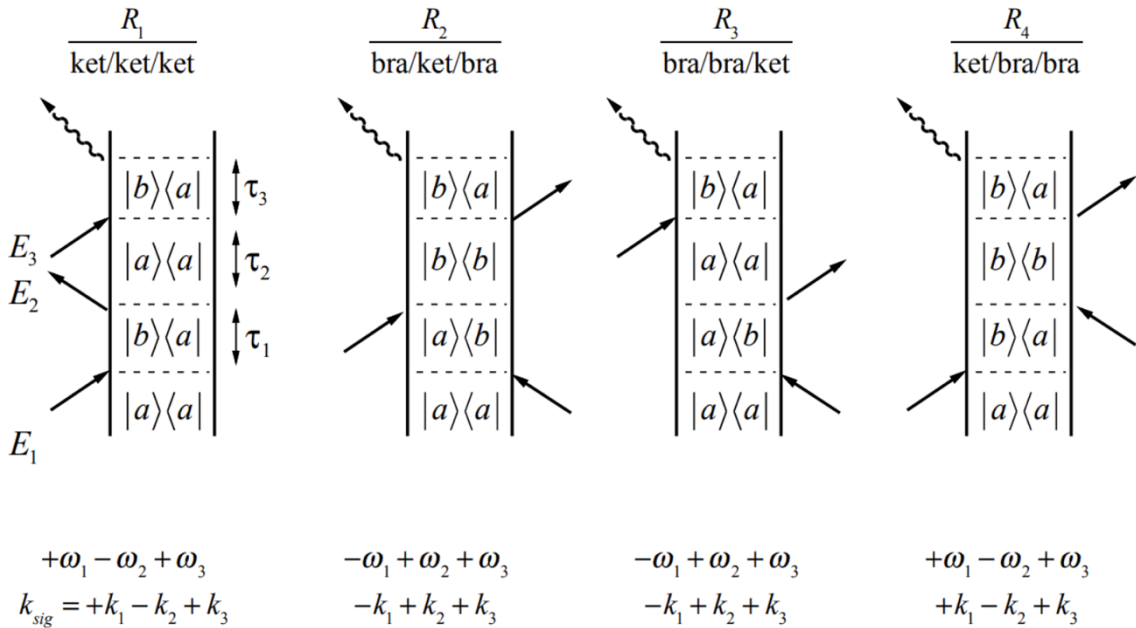

Figure 1.4: Example of a double-sided Feynman diagram for a multilevel system. Picture adapted from ref [7].

Feynman diagrams can be drawn by following a few fundamental rules:

1. The two double vertical lines represent the time evolution of the ket (on the left) and bra (on the right) side of the density operator.

2. The time evolution is upward.

3. Each light-matter interaction is represented by an arrow intersecting the diagram. Arrows pointing *towards* the diagram accounts for the absorption of light; arrows pointing *away* from the diagram represent instead an emission.

4. Before the first interaction with the field, the system is at the equilibrium in its ground state, whereas after the last interaction the system is left in a *population*, either ground or excited.

Given these few rules, we can now report the four Feynman diagrams necessary to describe the third order response function for a two-level system. It must be noted that the diagrams for the complex conjugate R_α^* are generally not displayed, since they are just the specular opposite of those for R_α.

R_1	R_2	R_3	R_4
ket/ket/ket	bra/ket/bra	bra/bra/ket	ket/bra/bra

$+\omega_1 - \omega_2 + \omega_3$ $\quad$ $-\omega_1 + \omega_2 + \omega_3$ $\quad$ $-\omega_1 + \omega_2 + \omega_3$ $\quad$ $+\omega_1 - \omega_2 + \omega_3$

$k_{sig} = +k_1 - k_2 + k_3$ $\quad$ $-k_1 + k_2 + k_3$ $\quad$ $-k_1 + k_2 + k_3$ $\quad$ $+k_1 - k_2 + k_3$

Figure 1.5: *Feynman diagrams representing the 3rd order nonlinear response function for a two-level system. R_1 and R_3 represent the ground state bleaching process, whereas R_2 and R_4 represent the stimulated emission. In a typical nonlinear spectroscopic experiment, the different contributions to the signal can be spatially separated according to specific combinations of the wavevectors **k**.*
Picture adapted from [6].

Among all the possible combinations, the most important contributions to the signal in a 2DES experiment are given by the *rephasing* (R) and *non-rephasing* (NR) signals, emitted along specific spatial directions:

$$\boldsymbol{k}_S^R = -\boldsymbol{k}_1 + \boldsymbol{k}_2 + \boldsymbol{k}_3 \tag{1.59}$$

$$\boldsymbol{k}_S^{NR} = +\boldsymbol{k}_1 - \boldsymbol{k}_2 + \boldsymbol{k}_3 \tag{1.60}$$

- The R_2 and R_3 terms evolve in conjugate coherences during t_1 and t_3, causing the phase acquired in t_1 to be reversed in t_3, resulting in the generation of an echo signal (*rephasing*).
- The R_4 and R_1 terms evolve in the same coherence state during t_1 and t_3, leading to a continuous acquisition of phase during both intervals (*non-rephasing*).

In Figure 1.5 we can distinguish between two different contributions to the signal:

- Diagrams R_2 and R_4 correspond to the stimulated emission (SE) process, where the first two pulses act differently on the bra and the ket, respectively, leading to an excited state population.
- Diagrams R_1 and R_3 instead refer to the bleaching of the ground state (GSB), a common phenomenon in time-resolved spectroscopies that accounts for the fact that the first two excitation pulses deplete the population of the ground state.
- If a second excited state is present, a third possible contribution that goes under the name of excited state absorption (ESA) could also contribute to the final signal. This contribution accounts for a pump-induced increased absorbance into the second excited state.

1.5.3 Fourth Order Population

Typically, when we talk about 2DES, we refer to the well-known "coherence-based" approach (Chapter 2, Section 2.1), which measures a coherent signal emitted left in a coherence after the interaction with the third pulse, as illustrated in Figure 1.5. However, alternative implementations of this technique that measure an incoherent signal have been developed [4-

9], as we will largely discuss in the following, since this variation is the focus of this dissertation. This approach, known as the "action-based" or "population-based" approach, is profoundly different from the previous one, since it no longer measures a coherent electric field but an incoherent fourth order signal, that originate from the final diagonal elements ρ^4_{kk} (i.e. excited state populations) of the density matrix. These populations are generated after four perturbations - and not three like in the case of the coherence-based approach. This fourth interaction is needed in order to convert the third order polarization into an excited state population, from which an incoherent signal of different nature (fluorescence, photocurrent or photoelectrons) is emitted [8-10]. Therefore, the signal is now proportional to a fourth order signal yield $Y^4(t)$, which, in analogy with Equation. 1.56, can be expressed as the convolution of four different fields with the fourth order response function $Q^4(t_4, t_3, t_2, t_1)$ [10]:

$$Y^4(t) = \int_0^\infty dt_4 \int_0^\infty dt_3 \int_0^\infty dt_2 \int_0^\infty dt_1 E(t - t_4)E(t - t_4 - t_3)E(t - t_4 - t_3$$
$$- t_2)E(t - t_4 - t_3 - t_2 - t_1)Q^4(t_4, t_3, t_2, t_1) \tag{1.61}$$

With

$$Q^4(t_4, t_3, t_2, t_1) = \left(\frac{i}{\hbar}\right)^4 \sum_{\alpha=1}^{8} [R_\alpha(t_4, t_3, t_2, t_1) - R_\alpha^*(t_4, t_3, t_2, t_1)] \tag{1.62}$$

This response function $Q^4(t_4, t_3, t_2, t_1)$ (Equation 1.62) is very similar to the the third order one, meaning that the fourth order signal emitted from incoherent populations still contains information about the coherent evolution of the quantum system, i.e. the system "remembers" the excitation path that led to the final population.

The fourth order response function contains 2^4=16 terms, which represent all the possible different Liouville pathways that contribute to the signal, which will not be reported here for brevity reasons. A more detailed treatment can be found in ref. [10].

The product of electric fields obtained from Equation 1.61 contains 8^4=4096 terms, which amounts to 4096×16=65536 different contributions if we also consider the complex conjugates. Given these premises, it is obvious that the number of terms is too large to deal with. Therefore, we must make some assumptions and approximations, in order to significantly reduce the number of terms that need to be taken into account. The first approximation we

make is to impose a strict time ordering of the four laser pulses ($t_1 < t_2 < t_3 < t_4$), whereas the second one consists in applying the *rotating wave approximation* (RWA) [6,11,12]. Let's consider the definition of the electric field in the exponential notation:

$$E(r,t) = \sum_{i=1}^{4} [E^+(r,t_i) + E^-(r,t_i)]$$

(1.63)

With $E^+(r,t_i) = A(t - t_i)e^{-i[\omega(t-t_i) - k_i \cdot r - \varphi_i]}$ and $E^-(r,t_i)$ the complex conjugate.

Since the action-based approach employs a fully collinear set up (meaning that the four laser pulses are sent along the same spatial direction and have the same wavevector k_i) we can neglect the wavevectors in the expression of the measured signal. We make use of the RWA to neglect one of the two components of each electric field (Equation 1.63), due to the fact that they contain opposite frequencies [6]. The remaining contributions differ depending on the way the laser pulses interact with the density matrix, as shown in Figure 1.6. These interactions can either occur from the left or right side of the Feynman diagram, contributing with a positive phase (resulting from $E^+(r,t_i)$) or a negative one (resulting from $E^-(r,t_i)$). The phase of the overall signal after the four interactions is given by the following expression [10]:

$$\varphi_s = \alpha\varphi_1 + \beta\varphi_2 + \gamma\varphi_3 + \delta\varphi_4$$

(1.64)

Where the coefficients $\alpha, \beta, \gamma, \delta \subset \mathbb{Z}$ represent the number and type of interaction of each of the four pulses with the density matrix.
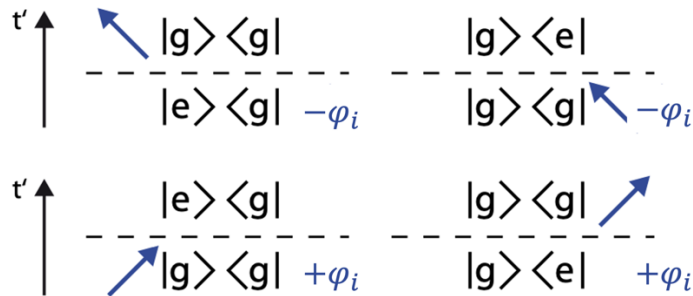
Figure 1.6*: Sign convention for the phase interactions with the density matrix. An arrow pointing to the left contributes with a negative phase $-\varphi_i$, whereas an arrow pointing to the right gives a positive contribution $+\varphi_i$. Picture adapted from [10].*

If we express the time-averaged fourth order signal

$$\overline{Y}^{(4)} = \int_{-\infty}^{+\infty} dt\, Y^{(4)}(t) \tag{1.65}$$

as a function of the relative time delays between the laser pulses, $t_1 = \tau_2 - \tau_1$, $t_2 = \tau_3 - \tau_2$, $t_3 = \tau_4 - \tau_3$, and their phases $\varphi_1, \varphi_2, \varphi_3, \varphi_4$, Equation 1.61 can be expressed as follows:

$$\overline{Y}^{(4)}(t_1, t_2, t_3, \varphi_1, \varphi_2, \varphi_3, \varphi_4) \tag{1.66}$$
$$= \sum_{\alpha, \beta, \gamma, \delta} \tilde{Y}^{(4)}(t_1, t_2, t_3, \alpha, \beta, \gamma, \delta) e^{i(\alpha\varphi_1 + \beta\varphi_2 + \gamma\varphi_3 + \delta\varphi_4)}$$

Where: $\tilde{Y}^{(4)}(t_1, t_2, t_3, \alpha, \beta, \gamma, \delta) e^{i(\alpha\varphi_1 + \beta\varphi_2 + \gamma\varphi_3 + \delta\varphi_4)}$ are the terms that sum over the fourth order response functions that survive the time ordering approximation and the RWA.

It is worth noting that each contribution to the signal with a specific total phase φ_s contains all the Liouville pathways Q_k with that phase dependency.

1.5.4 Rephasing and Non-Rephasing Contributions in Population-based Approach

The most interesting contributions to the signal in an ultrafast multidimensional optical experiment are without any doubt the rephasing and non-rephasing contributions, that we already mentioned for the coherence-based approach. Therefore, let's examine each contribution.

- Rephasing Contribution or *Photon Echo* (Figure 1.7): the rephasing signal has a total phase $\varphi_s = -\varphi_1 + \varphi_2 + \varphi_3 - \varphi_4$, and out of all the Liouville pathways that contains this contribution, only those that end in an excited state population are relevant and displayed in the Feynman diagrams. In analogy with the coherence-based approach, we can distinguish between the ground state bleaching (GSB), stimulated emission (SE) and excited state absorption (ESA). In the rephasing signal the density matrix is in a coherence during t_1 and t_3, and it oscillates with an opposite frequency during these two time intervals.

rephasing contributions
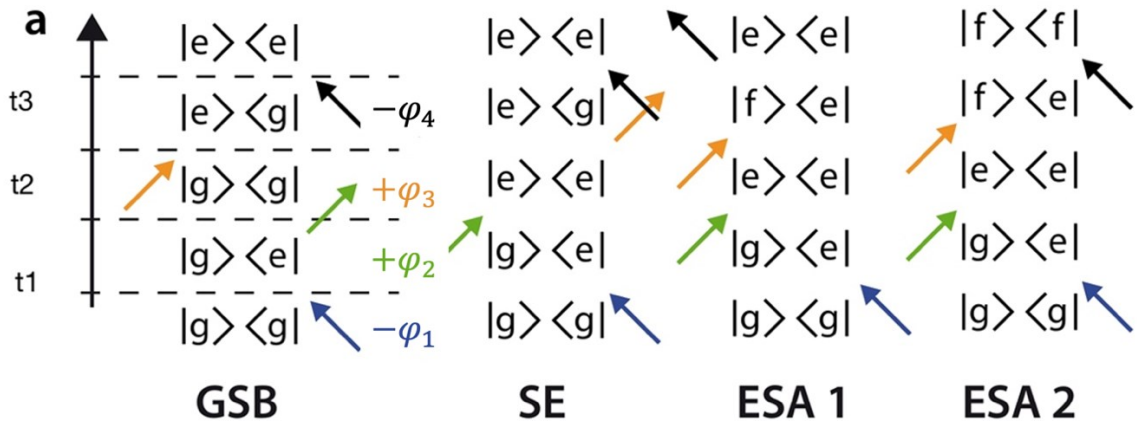
Figure 1.7: *Double-sided Feynman diagrams of Liouville pathways fulfilling the rephasing phase condition. Picture adapted from [10].*

- Non-rephasing contribution (Figure 1.8): in the non-rephasing contribution the density matrix is still in a coherence during t_1 and t_3 but it oscillates with a frequency of the same sign.
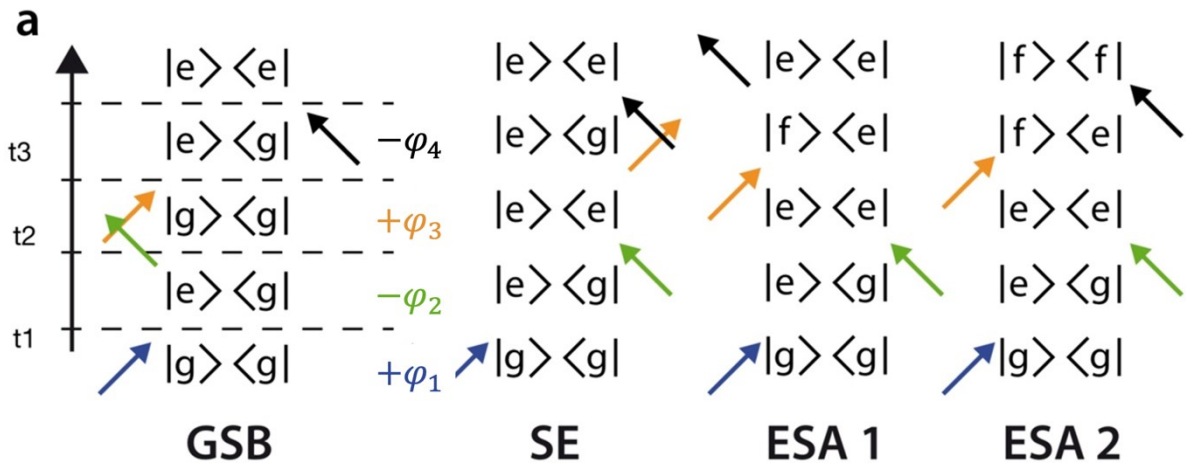
non-rephasing contributions

Figure 1.8: *Double-sided Feynman diagrams of Liouville pathways fulfilling the non-rephasing phase condition. Picture adapted from [10].*

Chapter 2
Coherent Two-Dimensional Electronic Spectroscopy

In Chapter 1, the mathematical formalisms that are necessary to understand and interpret the signals obtained in a 2DES experiment were presented. Once the theoretical background is acquired, it is now time to formally describe the technique in its whole complexity. Chapter 2 is therefore dedicated to an exhaustive treatment of the technique and will particularly focus on stressing the difference between the conventional coherence-based approach and the one employed in this dissertation, which goes under the name of "action-based approach".
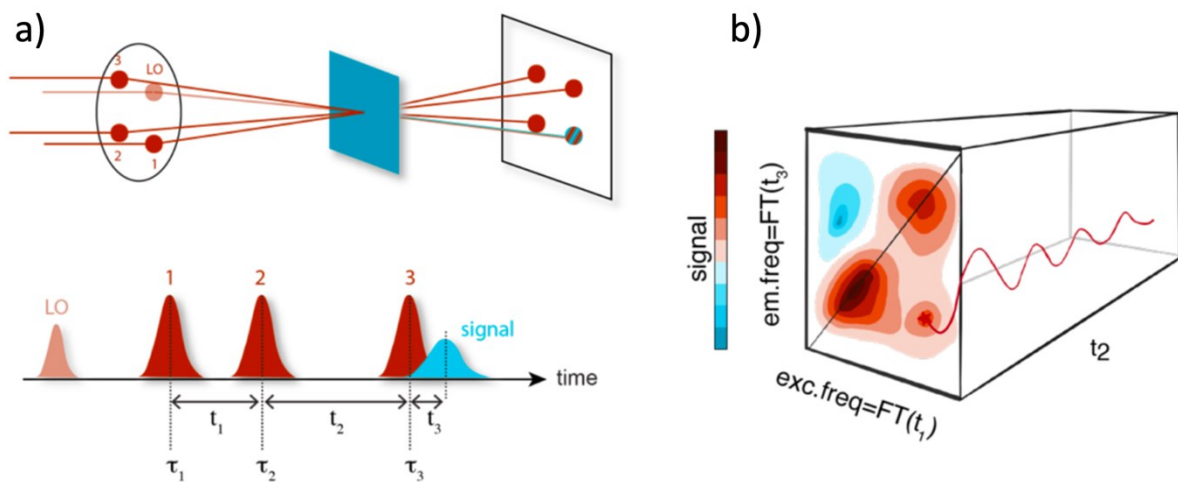
2.1 Coherence-detected 2DES

2DES is said to be a third order technique because the measured signal is proportional to the third order polarization (Equation 1.56). We already derived the analytical expressions for the experimental signal in terms of the third order response function $S^3(t_3, t_2, t_1)$, (see Equations 1.57-1.58). However, it is necessary to note that evaluating and interpreting this signal in the time domain is quite challenging. Therefore, due to the correlation of time and frequency *via* Fourier transform, we can easily obtain an expression for the third order response function in the frequency domain, where the signal can be evaluated more easily:

$$S^3(\omega_3, t_2, \omega_1) = \iint\limits_{0}^{\infty} dt_1 dt_3 S^{(3)}(t_3, t_2, t_1) e^{+i\omega_3 t_3} e^{\pm i\omega_1 t_1} \tag{2.1}$$

where $\pm$ stands for the rephasing and non-rephasing diagrams (Figure 1.5).

To understand how this signal is acquired, we must focus on how a 2DES experiment is performed. Given its wider popularity, we will now consider the case of the coherence-based approach, remanding to Section 2.2 of this chapter for the action-based variation.

The 2DES belongs to the class of four-wave mixing processes (FWM) that is performed by exciting the sample with a train of three non-collinear ultrashort laser pulses arranged in a BOXCARS geometry (Figure 2.1). The fourth wave is the signal generated after the interaction with the three exciting beams. Each incoming beam has its own spatial direction, characterized by a specific wavevector $\mathbf{k}$, and thus the different contributions to the signal (e.g. rephasing and non-rephasing contributions) can be selected by carefully choosing the geometry of incoming and detected beams, as well as the temporal ordering of the involved pulses (Chapter 1, Section 1.5.2) [13]. In addition to the sequence of the three exciting laser pulses, an additional beam is added, which acts as a local oscillator (LO) only for detection purposes (heterodyne detection).

Figure 2.1: *Experimental configuration for a coherence-detected 2DES experiment. (a) A train of three ultrashort laser pulses are sent non-collinearly to the sample in a BOXCARS geometry, where the three pulses are arranged on the three vertexes of a square. The signal emitted from the sample is detected in a direction which corresponds to the fourth vertex of the square, different from the exciting pulses' direction, ensuring a background free technique. (b)The final result of a 2DES measurements is a 3D matrix of data. Picture adapted from [4].*

Let's study the excitation scheme for a two-level system ($|g\rangle$ and $|e\rangle$). The first pulse at time τ_1 (Figure 2.1a) brings the system into a coherent state, which evolves during the coherence time t_1. The second pulse at τ_2 creates a population or a coherence (depending on the specific pathway), which relaxes over the population time t_2. Finally, the last pulse, arriving at time τ_3,

probes the system by creating again a coherence, from which a detectable electric field (the signal) is emitted at time t. The signal is recorded as a function of the time delays between the pulses that are systematically scanned throughout the experiment (Figure 2.1b). It is important to stress once again that specific excitation pathways, including the most important rephasing and non-rephasing processes, can be experimentally selected according to the exciting beams' geometry and temporal ordering.

The experimental signal is given as a stack of two-dimensional frequency-frequency correlation maps, each evaluated at a specific t_2 time (Figure 2.1b). The first dimension (i.e. the x axis) is obtained by scanning the time t_1, which is then Fourier-transformed into ω_1, named 'excitation' frequency. This axis depends on the first excited coherence and provides information on the energy associated with the states involved in the initially excited transition. The second dimension (i.e. the y axis), obtained by Fourier-transforming t_3 into the emission frequency ω_3, contains information about the second optical coherence, the one reached after the third pulse before the signal emission.

In light of this, it is clear that the position of the peaks, i.e., their (*x,y*) coordinates in a 2D map, depends on the interaction pathways between states and their dynamics [4]. For example, signals along the diagonals ($\omega_1 = \omega_3$) provide information on the excitonic structure of the system and correspond to the excitation spectrum. If a 2D map with only diagonal peaks is obtained, the system under investigation includes only non-interacting states. On the other hand, if a 2D map shows out-of-diagonal signals or "cross-peaks" ($\omega_1 \neq \omega_3$), this means that couplings between different excited states are established, like for example the coupling promoting energy transfer among two levels (Figure 2.2).

Not only the position but also the intensity and the shape of the peaks bring important information about the energy and the dynamics of the system.

The intensity of the peaks, like in many other spectroscopies, is proportional to the strength of the transition dipole moment, i.e. to the population change involved in such transition. The shape of the peaks accounts instead for the interactions of the system with the environment. In a typical 2DES experiment, as the time t_2 evolves, it is possible to observe a broadening and rounding of the peaks compared to the previous correlation maps. This phenomenon is known as "spectral diffusion" and accounts for the configurational changes in the local environment (Figure 2.3).
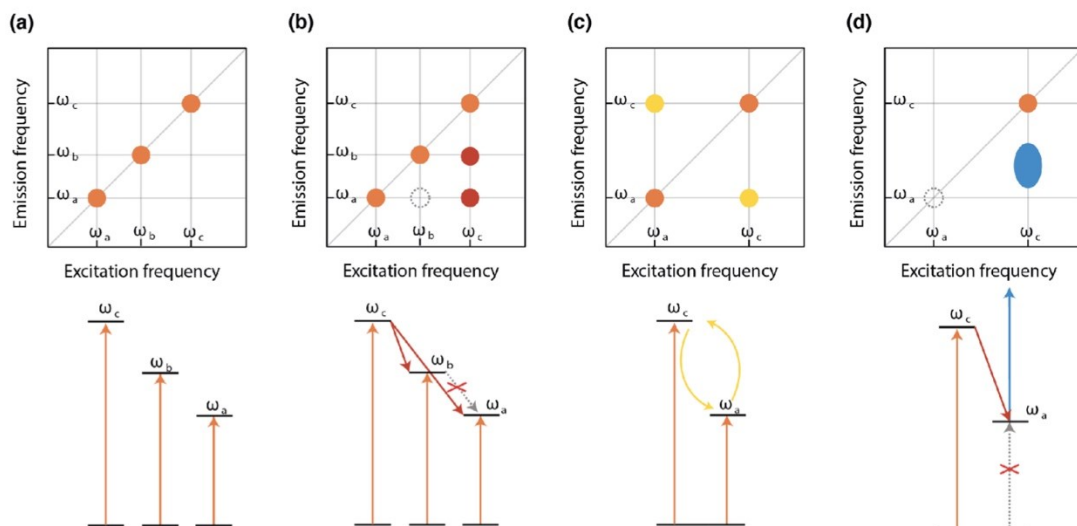
Figure 2.2: *The position of the peaks in 2D maps is strictly connected to the electronic structure of the sample. (a) Example of a non-interacting multi-level system, which displays peaks only along the diagonal. (b,c) Cross peaks appear in the case of coupling between excited states. In panel (b) the state c is coupled with states a and b via energy transfer, and cross-peaks appear at $t_2 > 0$. In panel (c) cross peaks already appear at $t_2 = 0$ at symmetric coordinates, signaling the presence of excitonic coupling like in an excitonic molecular dimer. (d) 2DES could also be useful in order to detect the presence of dark states, indirectly detected from their negative ESA signals (Chapter 1, Section 1.5.2). Picture adapted from [4].*
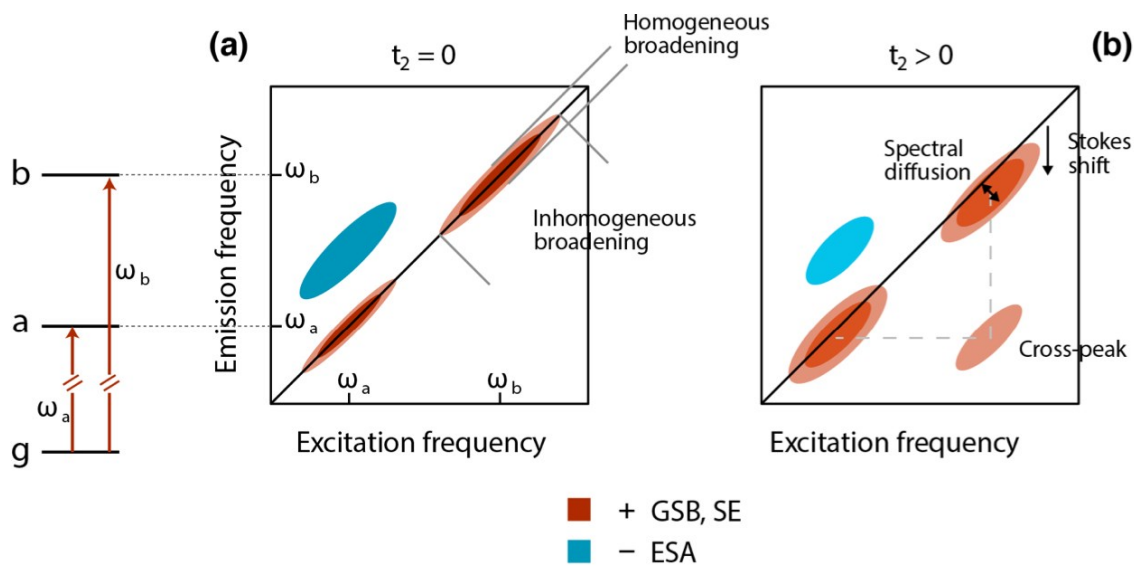
Figure. 2.3: *Pictorial representation of the signal evolution along t_2 for a multi-level system. At early population times (a) the peaks appear elongated along the diagonal, whereas as t_2 evolves (b), a broadening effect is recorded, due to the loss of correlation. Stokes shift could also take place due to the reorganization of the electronic clouds and solvent. Picture adapted from [4].*

2.1.1 Signal Evolution Along the Population Time

One last important aspect of the signal obtained from the 2DES technique is the evolution as a function of the population time t_2. In Chapter 1, Section 1.5.2, we showed that the signal is a sum of different contributions that can be visualized in terms of double-sided Feynman diagrams. These contributions can be grouped in two classes according to their different evolution during the time t_2 (Figure 2.4). The first group comprehends non-oscillating pathways, meaning that the signal evolves according to an exponential decay. These non-oscillating pathways are generated when the system reaches a pure state (or population) after the first two interactions. On the contrary, the second group consists of oscillating contributions that are generated whenever the system is left in a coherent superposition of states after the first two interactions with the light source. This beating contribution to the signal is described by a damped exponential function, whose oscillation frequency is proportional to the energy gap between the states involved in the superposition [4].
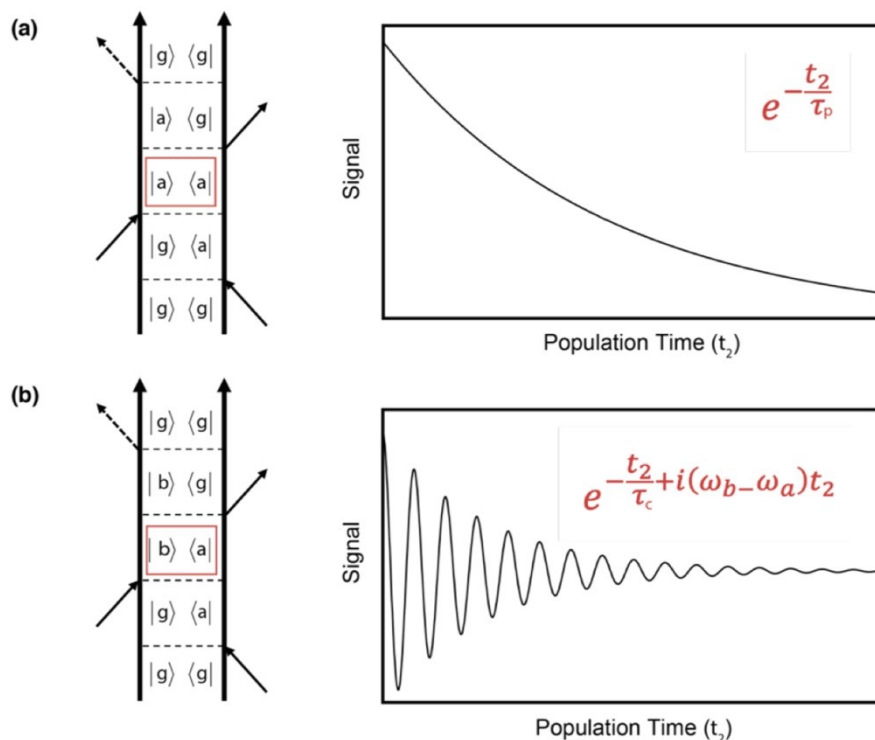

Figure 2.4: *a) Non-oscillating and b) oscillating contributions to the 2DES signal. Right panels illustrate the evolution of the signal according to the population time. τ_p and τ_c are the time constants associated to the population and coherence decays. Picture adapted from [4].*

2.2 Action-based Approach

In the previous section, we described the typical fully non-collinear configuration that is employed in coherence-based 2DES experiments. This approach is defined as 'coherence-based' because the final detected signal is a coherent electric field emitted by the sample in a well-defined spatial direction dictated by the phase-matching conditions.

However, in the last decade [5], different implementations have been developed. In particular, this dissertation focuses on the so-called "action-based" or "population-based" approach, which relies on a fully collinear set-up. In fact, in such kind of experiments, a sequence of four laser pulses is sent collinearly to the sample and induces the generation of an excited state population that relaxes back to the ground state emitting an incoherent signal (Figure 2.5).
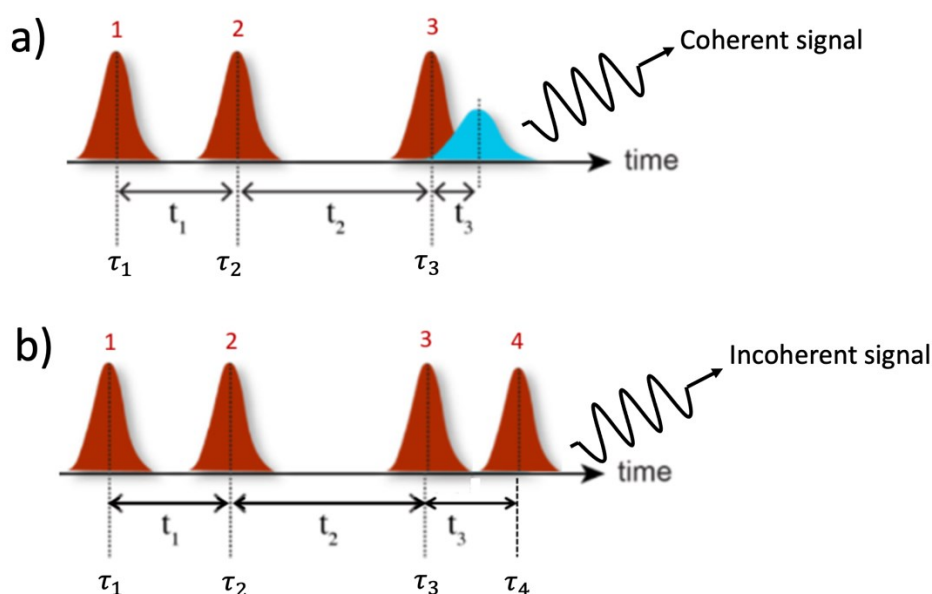
Figure 2.5*: Pictorial schemes of experimental set-ups for a) coherence-based vs. b) population-based approaches. a) As already seen above, in coherence-based approaches three laser pulses excite the sample and a fourth pulse (LO) is employed for heterodyne detection. The different contributions to the coherent signal can be distinguished according to their different spatial direction. b) Population-based approaches make use of collinear set-ups, where four laser pulses characterized by specific phases and time intervals are sent to the sample, which emits an incoherent signal. In this case, phase modulation or cycling schemes are employed for the selection of the signal.*

The addition of a fourth pulse is needed in order to leave the quantum system in a population state, from which an incoherent signal is emitted. However, the coherent information is not lost but is encoded in the exciting sequence [14]. This final state population can be probed according to different detection methods that are sensitive to photocurrent, fluorescence or photoions, depending on the nature of the sample. [5,10,15-17]

Action-based experiments have several advantages compared to coherence-based ones. First of all, they require a much simpler optical setup, as we will explain in more details in Chapter 4. Secondly, the signal emitted is a real property of the sample (e.g. fluorescence or photocurrent) and is not given by the interference of several electric fields. Properties such as fluorescence and photocurrent can be easily measured on the go while performing the experiment, thus enabling direct assessment of the sample under study. Lastly, it is important to mention that this approach offers an improved spatial resolution compared to the case of coherence-based approaches, especially applicable in the case of inhomogeneous solid-state samples, such as optoelectronic or quantum devices [4].

Because all the exciting beams are collinear, different contributions to the signal can no longer be disentangled with an appropriate detection geometry based on phase-matching considerations. Therefore, they must be unraveled according to methods that rely on the phase control, such as the *phase modulation* and the *phase cycling* techniques, that can be performed by an acousto-optic dispersive programmable filter (AOPDF) (Chapter 4, Section 4.4). Even though in the action-based approach the spatial information is lost, the different contributions to the signal can indeed be selected according to their phase dependence, in what is called a "phase-sensitive detection":

$$\varphi_s = \alpha\varphi_1 + \beta\varphi_2 + \gamma\varphi_3 + \delta\varphi_4 \qquad (2.1)$$

Where:

- φ_s is total the phase of the signal, given as a linear combination of the phases of the four collinear pulses,
- $\alpha, \beta, \gamma, \delta$ are coefficients that parametrize the different contributions to the signal.

2.2.1 Phase Modulation Techniques

The phase modulation technique is one of the two possible methods used in action-based approaches to disentangle the different contributions to the experimental signal. This method was pioneered by Marcus [18] and was implemented also in our setup [9], as described in Chapter 4.

In phase modulation techniques, the phase of each incoming beam is modulated at a frequency f_i. In this way, the final signal will include contributions modulated at different frequencies corresponding to linear combinations of the f_i [17-20].

In practice, the experiment is repeated by measuring the signal generated with different exciting pulse sequences (also labeled as 'pulses trains'). In each train, the four collinear pulses differ in their time delays and phases. The *m*-th train, made of four collinear laser pulses is written as [20]:

$$E^m(t) = \sum_{i=1}^{4} E_i^m(t) = E_1^m(t) + E_2^m(t) + E_3^m(t) + E_4^m(t)$$

(2.2)

Each pulse is described in terms of a Gaussian envelope and an oscillating function:

$$E_i^m(t) = E_i^0 exp\left\{-\frac{(t-\tau_i)^2}{2\sigma_i^2}\right\} \times \cos\left[\omega_i(t-\tau_i) + \varphi_i^m\right]$$

(2.3)

Where:
- E_i^0 is the electric field amplitude,
- σ_i is the duration of the pulse,
- ω_i is the carrier frequency,
- φ_i^m is the phase of the pulse in the *m*-th train.

The first pulse of each sequence is centered at τ_1, while the following pulses are delayed by specific time delays: $t_1 = \tau_2 - \tau_1$, $t_2 = \tau_3 - \tau_2$, and $t_3 = \tau_4 - \tau_3$.

As anticipated before, the phase φ_i^m of each pulse is modulated at a frequency f_i.

The recorded signal is then Fourier Transformed along t. Each individual peak appearing in the resulting spectrum is characterized by a unique modulation frequency, denoted as f_s, which is a linear combination of the modulation frequencies f_i.

In fact, every peak observed in the phase-modulation spectrum corresponds to a signal generated through a series of excitation pathways brought about by distinct interactions with the laser pulses and corresponds to a specific frequency. For example, the contributions of the rephasing and non-rephasing will be modulated at the following frequencies:

$$f_{s,rephasing} = -f_1 + f_2 + f_3 - f_4$$
$$f_{s,non-rephasing} = +f_1 - f_2 + f_3 - f_4$$

Even though this procedure may seem complex and time-consuming, it has the essential advantage of simultaneously collecting all the different contributions to the signal, including the well-known rephasing and non-rephasing, but also higher terms.

The choice of the phase modulation frequencies f_i is, therefore, a key parameter in order to select the desired components contributing to the signal. The phase-modulation scheme employed in this work will be described in Chapter 4, Section 4.4.

In conclusion, the phase-modulation technique is a powerful tool in the context of action-based 2DES, since it offers a dynamic approach to manipulate and control the temporal and spectral characteristics of laser pulses. By introducing controlled variations in the phase relationships between pulses, phase modulation is useful for extracting rich information about the incoherent signal. The adaptability of phase modulation schemes allows for tailored and flexible experiments, in order to address specific aspects of interest in the sample under study.

2.2.2 Phase Cycling Techniques

The second approach that could be used to extract the desired signal component involves the utilization of phase cycling [14]. In this method, a pulse shaper is employed to generate a sequence of four laser pulses with fixed phases, allowing for the exploration of various phase combinations while capturing the signal for each configuration. In phase cycling schemes, controlled rotations are applied *independently* to the phases of the excitation pulses. Spectra are obtained for various phase combinations, and subsequently

merged to eliminate signals unaffected by the phase of all three excitation pulses, as predicted by the response function theory. Like phase modulation, also this technique allows us to discard the spatial separation of pulses in favor of phase separation and significantly simplifies the optical set-up. However, since this signal-selection scheme was not employed in this work, we will not further describe it. For additional information about the phase cycling, we remand to ref. [14].

Chapter 3
Quantum Dots

Quantum Dots (QDs) are semiconductor nanocrystals that have gained large popularity over the last few decades because of their unique size-dependent optical and opto-electronic properties. Their applications span many fields, from everyday uses, such as QLEDs-based television and smartphone screens, to more sophisticated applications, such as photovoltaics, lasing and bio-imaging [21-24].

The primary characteristic of these nanocrystals is, in fact, associated with their size: since their diameter is small compared to the average length scale of electron-hole pairs, known as the Bohr radius a_{ex}, the electron and the hole wavefunctions undergo a three-dimensional *quantum confinement*, which experimentally results in the discretization of the electronic energy levels, as observed in their absorption spectrum [25]. Because of their dimensions, they are often seen as a connection between the macroscopic world of bulk materials and the microscopic realm of molecular systems.

QDs of several materials are available. The most common ones are typically based on Cd and chalcogenides, such as CdSe, CdS, CdTe; Pb-based alternatives with chalcogenides, like PbS, and PbSe are also widespread. However, health hazards related to acute toxicity of Cd and Pb are orienting the synthetic research towards less toxic and more environmentally friendly compounds, such as InAs, InP, ZnSe, GaAs [26].

Despite the just mentioned health-dangers ascribed to these elements, we still decided to employ a CdSe-based opto-electronic device and to characterize it by the means of action-based 2DES. This choice might seem to be in contrast with what said above, however, the unique optical and electronic properties of CdSe-based QDs and the fact that they are very well characterized in terms of photophysical properties make them a valuable option for our purposes, thus prioritizing their experimental advantages rather than their toxicity-related hazards.

3.1 Quantum Dots and Excitons

In order to better understand the unique properties of QDs, it is important to familiarize with the electronic structure of semiconductor materials and the concept of exciton. In a typical bulk semiconductor material, electronic states are so close to each other in energy that these electronic levels are no longer treated as discrete levels but rather like bands. According to the band theory, in semiconductor crystals it is possible to distinguish between a valence band, populated at 0 K, and a conduction band, which is not populated at 0 K [27]. These two bands are separated by an energy gap, referred to as "bandgap", which is characteristic of the semiconductor material. Upon absorption of thermal energy or photons, some electrons can gain a sufficient amount of energy to transition from the conduction to the valence band. This promotion leads to the formation of an exciton (Figure 3.1). Indeed, the electron located in the conduction band, which is negatively charged, is electrostatically bound to the *hole*, i.e. the vacancy bringing a formal positive charge in the valence band, generated by the loss of that electron.
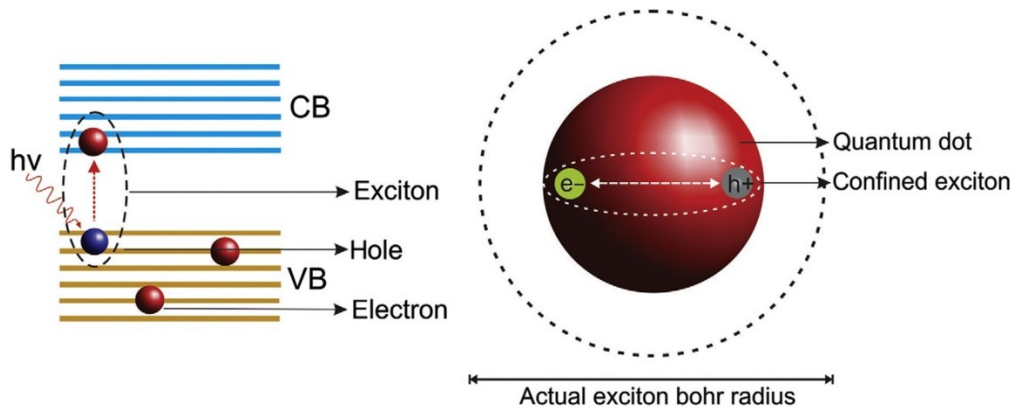
Figure 3.1*: On the left, the formation of an exciton is depicted. On the right, a comparison between the excitonic Bohr radius vs. the QD diameter is sketched. Picture adapted from [28].*

These excitons are characterized in terms of the spatial distance between the electron and the hole, which is called the excitonic Bohr radius:

$$a_{ex} = \frac{4\pi\varepsilon\hbar^2}{\mu e^2} = \varepsilon \frac{m_e}{\mu} a_0, \qquad\qquad (3.1)$$

Where:

- ε is the dielectric constant of the material,

- $\hbar$ is the reduced Planck's constant,

- μ is the reduced mass of the excitonic pair: $\mu = \frac{m_e m_h}{m_e + m_h}$,

- m_e is the rest mass of the electron,

- a_0 is the Bohr's radius of the hydrogen atom: $a_0 = \frac{4\pi\varepsilon_0 \hbar^2}{m_e e^2} = 0.0529$ nm.

Two different kinds of excitons can be distinguished according to the value of the dielectric constant ε: the Wannier-Mott and Frenkel excitons [29,30].

The Wannier-Mott exciton is typical of semiconductor materials characterized by a large value of the dielectric constant. In fact, if ε is large, the Coulombic interaction between the electron and hole pair will be weakened because of the screening effect, thus increasing the value of the excitonic Bohr radius. High values of the Bohr radius are indicative of the possible delocalization of the exciton inside the crystalline lattice. On the contrary, in Frenkel excitons, which are typical of materials characterized by a small value of the dielectric constant, the Coulombic interaction is not significantly affected by any screening effect. As a result, Frenkel excitons typically have small Bohr radii and tend to remain confined within the crystalline site where they were generated.

By substituting the values of the masses of the electron and the hole into Equation 3.1, we can easily obtain the Bohr radii for these particles, a_e, and a_h, for the electron and the hole, respectively. Therefore, by comparing these values with the radius a of a nanocrystal, it is possible to identify three different regimes for the particle's confinement [31,32]:

1. $a_e, a_h < a < a_{ex}$: the *weak confinement regime* suits the case of larger nanocrystals, where only the centre of mass of the electron is spatially confined.
2. $a_h < a < a_e, a_{ex}$: in smaller nanocrystals a is typically intermediate between a_h and a_e, meaning that in this *intermediate confinement regime* only the electron is strongly confined, whereas the hole is not.
3. $a < a_{ex}, a_e, a_h$: for even smaller nanocrystals, both the electron and the hole are strongly confined. This is the case of the *strong confinement regime*.

In this thesis, CdSe QDs with an average diameter of 3.7 nm were studied. The excitons formed within this diameter range lay in the strong confinement regime since the excitonic Bohr radius is approximately 5.4 nm, significantly larger than the diameter of the single QD [33-35]. In these conditions, quantum confinement effects arise, and thus the electronic structure of these nanomaterials is no longer characterized by a continuum of levels but by discrete levels [28]. The effect of quantum confinement becomes more relevant as the size of the QD decreases [23].

3.2 Electronic Structure of QDs

Since the electronic structure of QDs is characterized by the presence of discrete energy levels due to quantum confinement effects, an *ad hoc* description of these unique materials is needed. A simple and intuitive approach that is particularly appropriate to describe the electronic structure of QDs is the particle-in-a-sphere (PIS) model, which is a good approximation when no defects nor surface irregularities are present on the surface of the dot.

We will start our description from the band theory applied to the case of bulk CdSe, and then we will scale down to the case of CdSe QDs.

In the case of the bulk material, Cd and Se atoms are arranged in a three-dimensional crystalline lattice, and the individual states describing these particles can be obtained by solving the time-independent Schrödinger equation[3] [36,37]:

$$\left(\frac{-\hbar^2 \nabla^2}{2m} + U(\boldsymbol{r}) \right) \psi(\boldsymbol{r}) = E \psi(\boldsymbol{r}) \tag{3.2}$$

Where:
- ∇^2 is the Laplace operator, defined as: $\nabla^2 = \frac{\partial^2}{\partial x^2} + \frac{\partial^2}{\partial y^2} + \frac{\partial^2}{\partial z^2}$,
- m is the mass of the single particle,
- $U(\boldsymbol{r})$ is the periodic potential.

---

[3] Please note that in Equation 3.1 the Hamiltonian has been split into a kinetic term and a periodic potential.

In condensed state physics, the solution to Equation 3.2 can be written as a plane wave modulated by a function $u(\boldsymbol{r})$ with the same periodicity as the crystal lattice, according to Bloch's theorem [27]:

$$\psi(\boldsymbol{r}) = u(\boldsymbol{r})\varphi(\boldsymbol{r}) = u(\boldsymbol{r})e^{i\boldsymbol{k}\cdot\boldsymbol{r}} \tag{3.3}$$

Where the function $\varphi(\boldsymbol{r})$ is known as the *envelope function*.

The energy associated with these wavefunctions can be represented in a band diagram, in which the energy is reported as a function of $\boldsymbol{k}$, the reciprocal-lattice vector. According to the *effective mass approximation* (EMA), each one of these bands is described by a parabolic function and the effective mass incorporates the periodic potential perceived by the particle within the crystalline lattice. In our case, since CdSe is a direct gap semiconductor, both the maximum of the valence band and the minimum of the conduction band are located at $\boldsymbol{k} = 0$ [36].

Within the EMA, it is possible to solve Equation 3.2 in order to obtain an expression for the energy associated to the individual states [32]:

$$E_k^e = \frac{\hbar^2 \boldsymbol{k}^2}{2m_{eff}^e} + E_{gap} \tag{3.4}$$

$$E_k^h = -\frac{\hbar^2 \boldsymbol{k}^2}{2m_{eff}^h} \tag{3.5}$$

Where:

- $\boldsymbol{k}$ is the wavevector of the particle, defined as $\boldsymbol{k} = \frac{\pi}{a}n$, where n is a set of integers that define the direction of the wavevector: $n = (n_1, n_2, n_3)$, where (n_1, n_2, n_3) are the Miller indexes,
- m_{eff}^h and m_{eff}^e are the effective masses for the hole and electron, respectively,
- E_{gap} is the energy gap between the valence and conduction band.

These solutions are suitable for the general case of a bulk semiconductor material, and we will now take into consideration the case of the nanocrystal.

We will start our treatment by first assuming that the diameter of the nanocrystal is much larger than the lattice constant of the material. If this assumption is valid, we can make use of the *envelope function approximation* (EFA), according to which the wavefunction of the particle can be expressed as a linear combination of Bloch functions [36]:

$$\psi(\boldsymbol{r}) = \sum_k C_{nk} u_{nk}(\boldsymbol{r}) e^{i\boldsymbol{k}\cdot\boldsymbol{r}} \tag{3.6}$$

Where C_{nk} are the expansion coefficients satisfying the spherical boundary conditions for the nanocrystal.

In the case of a weak dependence on $\boldsymbol{k}$, the function $u_{n0}(\boldsymbol{r})$, that is the Bloch function relative to $\boldsymbol{k} = 0$, can be rewritten, within the *tight binding model* or LCAO approximation, as:

$$u_{n0}(\boldsymbol{r}) \cong \sum_j C_{nj} \varphi_n(\boldsymbol{r} - \boldsymbol{r}_j) \tag{3.7}$$

Thus, Equation 3.6 becomes:

$$\psi(\boldsymbol{r}) = u_{n0}(\boldsymbol{r}) \sum_k C_{nk} e^{i\boldsymbol{k}\cdot\boldsymbol{r}} = u_{n0}(\boldsymbol{r}) f_{sp}(\boldsymbol{r}) \tag{3.8}$$

Where:

- φ_n are the atomic wavefunctions,
- f_{sp} is the envelope function for the single particle.

To provide an exhaustive treatment of this problem, this latter function f_{sp} must now be determined. To this aim, it is possible to exploit the *particle in a sphere model* (PIS), which provides a quantum description of a particle inside a spherical potential well of radius $\boldsymbol{a}$. Within this model, the potential energy $V(\boldsymbol{r})$ is defined as:

$$V(\boldsymbol{r}) = \begin{cases} 0, & 0 \leq \boldsymbol{r} < \boldsymbol{a} \\ \infty, & \boldsymbol{r} > \boldsymbol{a} \end{cases} \tag{3.9}$$

In the case of $0 \leq \boldsymbol{r} < \boldsymbol{a}$, the particle is free to move within a confined region of space. The associated wavefunctions are obtained by solving the time-independent Schrödinger equation and assume the following expression [36,37]:

$$\Phi_{n,l,m}(\boldsymbol{r},\vartheta,\phi) = C \frac{j_l(k_{n,l},\boldsymbol{r})Y_l^m(\vartheta,\phi)}{r} \tag{3.10}$$

Where:

- C is a normalization constant,
- $Y_l^m(\vartheta,\phi)$ is the spherical harmonic,
- $j_l(k_{n,l},\boldsymbol{r})$ is the l-th order spherical Bessel function[4], with $k_{n,l} = \frac{\alpha_{n,l}}{a}$ ($\alpha_{n,l}$ is the n-th zero of j_l).
- n, l, m are the quantum numbers.

The expression of the energy associated with these particles is given by:

$$E_{n,l} = \frac{\hbar^2 \alpha_{n,l}^2}{2m_0 a^2} = \frac{\hbar^2 k_{n,l}^2}{2m_0} \tag{3.11}$$

Where m_0 is the mass of the particle.

In the case of spherical nanocrystals, the envelope functions $f_{sp}(\boldsymbol{r})$ are obtained by solving Equation 3.10 for the particle in a sphere. In this view, electron and hole levels can be described in terms of an atomic-like orbital confined inside the nanocrystal, whose energies are determined by the simple substitution of their effective masses m_{eff}^h and m_{eff}^e into Equation 3.11.

In the last step of this treatment, we will finally take into account the Coulombic attraction between the hole and the electron, i.e., the excitonic interaction. In the strong confinement regime, the hole and the electron can be treated separately, and the Coulombic interaction can be described as a first-order correction to the energy, according to the fact that the dependence of the confinement energy of the carriers is greater than the electrostatic potential [36]. The former, in fact, scales with $1/a^2$, whereas the latter with $1/a$. We can finally write the excitonic states for a nanocrystal as:

---

[4] Bessel functions are canonical solutions of the Bessel's differential equation and are typically invoked when solving problems in which cylindrical or spherical coordinates are involved.

$$\Psi_{ex}(\boldsymbol{r}_e, \boldsymbol{r}_h) = \Psi_e(\boldsymbol{r}_e)\Psi_h(\boldsymbol{r}_h) = u_c f_e(\boldsymbol{r}_e)u_v f_h(\boldsymbol{r}_h) \tag{3.12}$$

$$= C \left[u_c \frac{j_{L_e}(k_{n_e,L_e}\boldsymbol{r}_e)Y_{L_e}^{m_e}}{\boldsymbol{r}_e} \right] \left[u_v \frac{j_{L_h}(k_{n_h,L_h}\boldsymbol{r}_h)Y_{L_h}^{m_h}}{\boldsymbol{r}_h} \right]$$

With energies [30]:

$$E_{ex}(n_h L_h n_e L_e) = E_g + \frac{\pi\hbar^2}{2\mu a^2} - 1.8\frac{e^2}{\varepsilon a} \tag{3.13}$$

Where:

- n, L are the principal and azimuthal quantum numbers for the hole and the electron,
- μ is the reduced mass for the excitonic pair.

From Equation 3.13, according to the dependence of the expression on a, it is easy to deduce that the energy gap of the nanocrystal will always increase when decreasing its diameter. Consequently, as the size decreases, the absorption spectrum will be shifted towards shorter wavelengths, i.e., it will be "blue-shifted", due to the quantum confinement of the wavefunction (Figure 3.2).
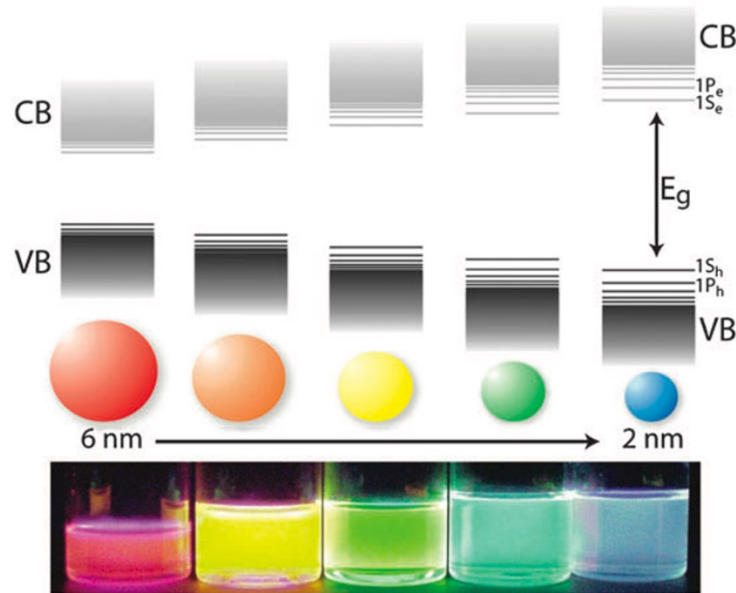
Figure 3.2: The influence of size on the energy gap value. As the dot becomes smaller and its diameter decreases, the energy gap between the valence and conduction band will rise. This aspect is of fundamental importance in synthetic approaches: in fact, by carefully controlling the dimensions of the dots it is possible to precisely control the band gap of the semiconductor nanocrystals. Picture adapted from [38].

When studying the discretization of energy states resulting from spatial confinement, a useful parameter is the density of states (DOS), that accounts for the number of electrons having energies between E and $E + \Delta E$. The density of states $\rho(E)$ is a function of the dimensionality (Figure 3.3) [37,39]:

$$\rho(E) \propto E^{(d-2)/2} \quad d = 1,2,3. \tag{3.14}$$
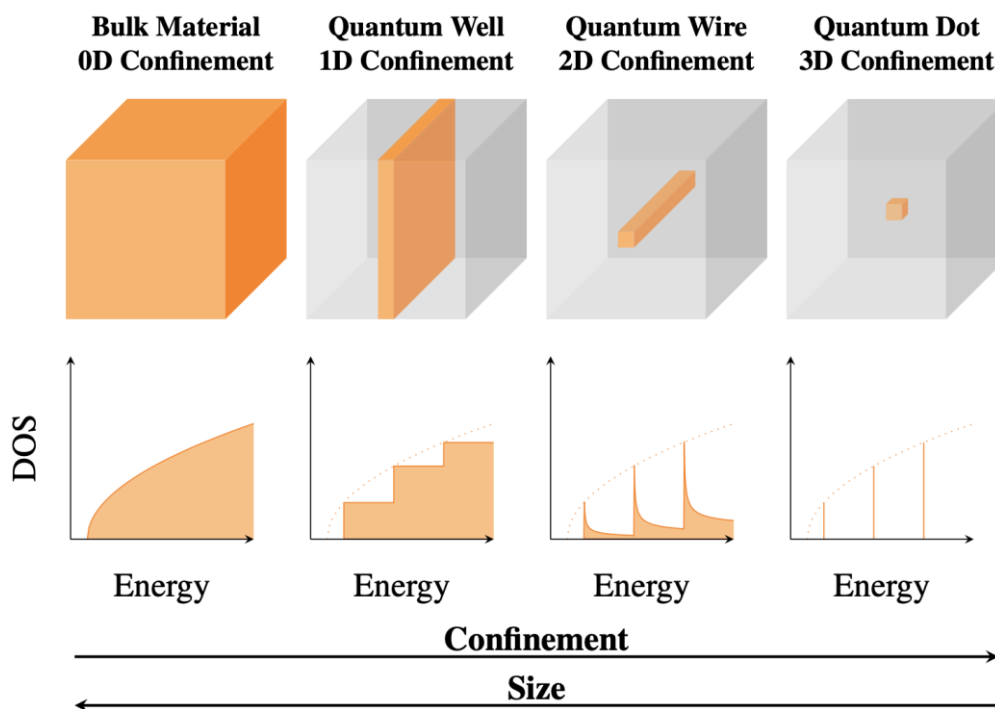
Figure 3.3: *Density of states (DOS) as a function of energy, from bulk materials to 3D confined nanocrystals.*

Let's now examine in detail the electronic band structure for a bulk zincblende CdSe semiconductor (Figure 3.4) obtained thanks to a $k \cdot p$ perturbation method[5] [27,40].

---

[5] $k \cdot p$ perturbation method relies on the description of the energy states of the hole using the Luttinger Hamiltonian [41] and the energy states of the electron using the Kane Hamiltonian [42,43].
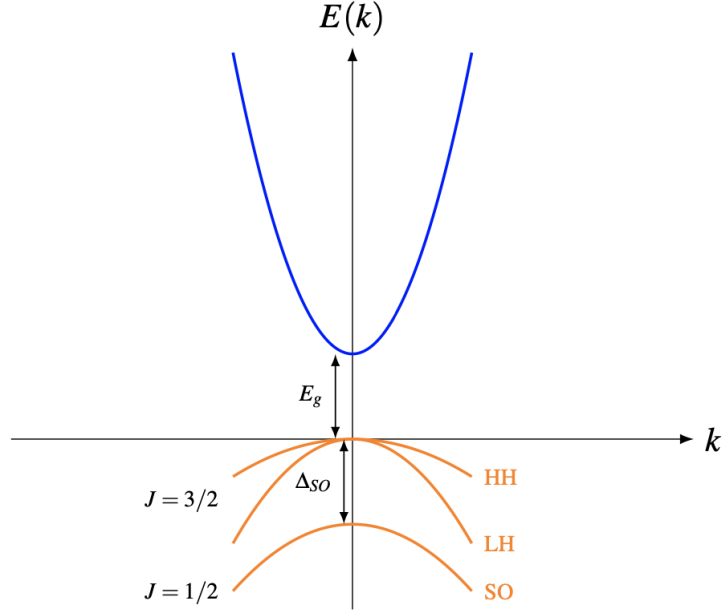
**Figure 3.4**: *Qualitative band structure of bulk zincblende CdSe.*

The conduction band arises from the empty *5s* orbitals of Cd, it is 2-fold degenerate and can be described by a single band near $k = 0$. On the contrary, the valence band derives from the Se *4p* orbitals and is represented in terms of three different bands, the heavy-hole (HH), the light-hole (LH) and the split-off (SO) bands, as depicted in Figure 3.4. These three bands result from linear combinations of Se *4p* atomic orbitals, initially showing sixfold degeneracy at $k = 0$. Upon introducing strong spin-orbit coupling (SOC) (which has a theoretical value of 0.42 eV for the case of CdSe semiconductor [44,45]), these valence bands are split into two sub-bands ($p_{3/2}$ and $p_{1/2}$). Each valence band is labeled by its total angular momentum $J = l + s$, where l is the orbital angular momentum, and s is the spin momentum. In addition, when moving away from $k = 0$, the $p_{3/2}$ band further splits into LH and HH sub-bands. When dealing with QDs, the hole states within the valance are mixed with each other, resulting in a mixing effect that must be taken into consideration. This mixing effect is responsible for the fact that L_h and J are not preserved, whereas the total angular momentum of the hole and the parity are maintained, giving rise to the S-D mixing. Therefore, QD hole states can be denoted as $n_h L_F$, where the letter F refers to the total angular momentum. Differently from the valence band, the conduction band remains unaffected and is labeled as $n_e L_e$. According to this notation, the first excited state is named as $|1S_{3/2}1S_e\rangle$ or simply $|1S\rangle$. The second excited state

is referred to as $\left|2S_{3/2}1S_e\right.\rangle$ or $\left|2S\right\rangle$, and the same notation holds for the following excited states (Figure 3.5).
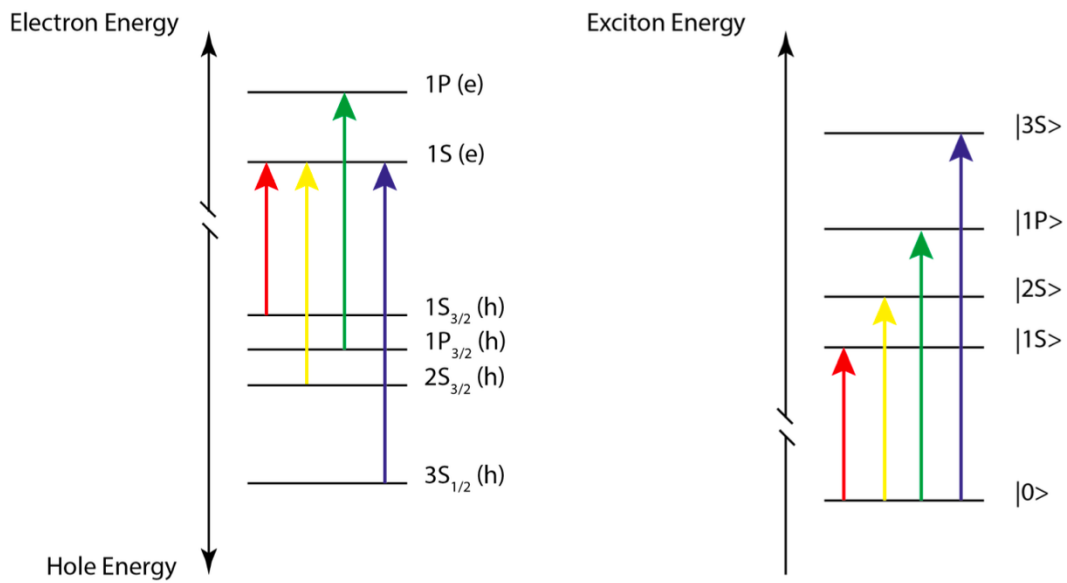
Figure 3.5*: Representation of the first four excited pair states of CdSe QDs, in the electron-hole (left) and excitonic (right) views.*

Figure 3.6 depicts the allowed transitions as identified by Norris and Bawendi through a careful comparison between theoretical predictions and photoluminescence data [25]. According to their work, the mixing effect is not enough to explain the photoluminescent properties of these nanocrystals and, therefore, also the band-edge fine structure of the exciton must be considered.
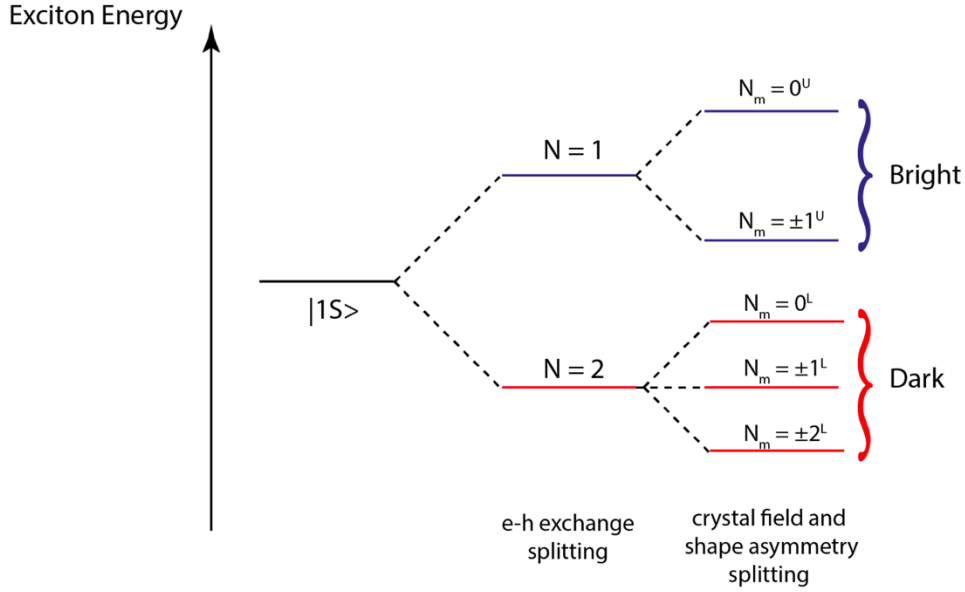
Figure 3.6: *Exciton fine structure at the band edge involves the splitting of the 8-fold |1S⟩ exciton due to electron-hole exchange. This results in two states with total angular momentum N: one with N equal to 1 (for the 3-fold degenerate) and the other with N equal to 2 (for the 5-fold degenerate). The bright state is associated with the upper level, while the dark state gives rise to the exciton band in photoluminescence spectra, upon phonon-assisted activation. Crystal field effects are the second reason why degeneracy is partially removed, leading to the separation of states labeled U (upper) and L (lower) depending on the magnitude of Nm. This picture is adapted from [36] and it is not in scale.*
The energy difference between the absorption and emission spectra's band edge peaks is called the non-resonant (global) Stokes shift, whereas the resonant Stokes shift refers to the energy gap between the lowest-energy absorbing state and the emitting state [46].

The splitting of the |1S⟩ state, which exhibits an 8-fold degeneracy, arises because of the presence of two different interactions:

- The presence of strong exchange interactions between electrons and holes,
- The presence of anisotropies associated with the crystal field.

In the presence of the quantum confinement effect, the overlap between the electron and hole wavefunctions is enhanced, thus making the electron-hole exchange splitting non-negligible, differently from the case of bulk materials. Consequently, the electron and hole states forming the band edge exciton must be treated as a combined exchange-correlated exciton.

This exciton is characterized by a total angular momentum, N, with possible values of 1 or 2, depending on the linear combination of the angular momenta of individual carriers. It follows that the energy associated with these split states can be calculated as eigenvalues of the exchange Hamiltonian.

The upper state, characterized by $N = 1$, is 3-fold degenerate, whereas the lower one, characterized by $N = 2$, is 5-fold degenerate. However, this degeneracy can be partially

removed if shape asymmetries (i.e. anisotropies) are present (Figure 3.6). The energy gap between $N_m = \pm 2^L$ and $N_m = 0^L$ corresponds to the resonant Stokes shift, which can assume a value in the range 1-10 meV, depending on the dimensions of the QD. However, this contribution to the global Stoke shift is typically smaller than the one deriving from the energy gap between $N_m = \pm 1^U$ and $N_m = 0^U$, which ranges from 20 up to 80 meV.

3.3 QDs Dimers

In light of the electronic properties described before, QDs have also been defined as 'artificial atoms' [47-49]. This definition inspired the formation of QDs meso-structures like dimers, trimers etc. [50]. Whenever the distance between two different quantum dots (QDs) is sufficiently small, they can interact via the Coulomb potential, giving rise to the formation of stable QD dimers. Within these dimers, each one of the four bands of excitons associated with one dot (Dot A in Figure 3.7) couples with the bands of excitons of the other dot (Dot B in Figure 3.7) through an inter-particle Coulomb coupling. The coupling between two different dots leads to the formation of new *eigenexciton* states that are *delocalized* over the two dots forming the dimer (Figure 3.7).
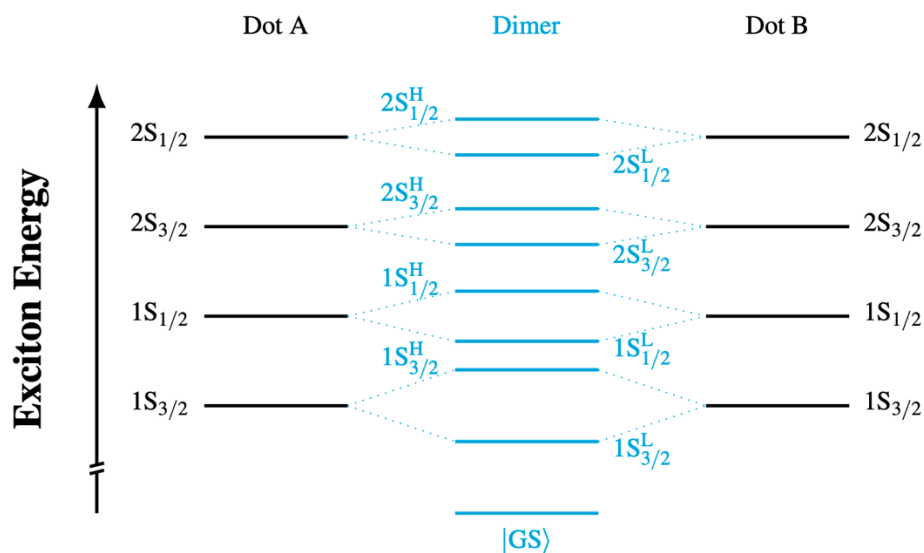
Figure 3.7: *Fine electronic structure of a dimer of QDs with a mean diameter D<3.2 nm. Picture adapted from [36].*

Therefore, out of one exciton band localized within each QD, two exciton bands emerge in the dimer, labeled as "low energy" (L) and "high energy" (H), which are separated by an amount of energy that is approximately twice the strength of the inter-dot Coulomb coupling [44].

In summary, each QDs dimer exhibits eight *eigenexciton* bands, as illustrated in Figure 3.7. In light of this, the dimer displays a distinctive fine structure composed of 48 different states. According to this different electronic structure, one can expect that the dimer will display linear and nonlinear optical spectra different from the monomer.

The formation of delocalized hybrid states in dimers imparts to the nanosystems peculiar electronic and optical properties and novel functionalities relevant to numerous applications, including quantum technologies [4].

Previous work by our group allowed characterize with great detail the electronic properties of QDs in their monomeric and dimeric forms, both in solutions and in solid-state films [44,45,51]. In these works, coherence-based 2DES measurements were employed to characterize the ultrafast dynamics of QDs dimer samples, revealing exciting quantum coherent behavior dominating the early steps of the relaxation dynamics. These findings also lead to the proposal of a first example of a quantum technology application based on the 2DES data collected on QDs samples [52].

3.4 Sample Preparation

Although detecting quantum coherent behavior in QD dimers is interesting from a fundamental knowledge standpoint, it is reasonable to question whether these properties can be effectively utilized in a real device. In other words, does quantum coherence truly impact the final functionality of a QD-based device? To address this question, we chose to shift from a coherence-based approach to an action-based approach in this thesis. This allowed us to directly characterize the ultrafast (possibly coherent) dynamics of a functioning device. We specifically focused on photocurrent-detected properties in view of a wealth of experimental data available on the static photocurrent characteristics of QD materials dating back to the 90s [25].

However, the use of a photocurrent-detected scheme poses the first relevant challenge faced in this work: the design of the sample, which must be conductive.

The sample that was investigated in this thesis was created through a collaborative effort. Dr. Marinella Striccoli (CNR-IPCF, Bari) synthesized the QDs and deposited them, while the group of Prof. Jan Mol (Queen Mary University of London) was responsible for the device preparation, wiring, and encapsulation.

The main component of the device is a thin layer of colloidal CdSe QDs deposited over interdigitated gold plates, which are electronically connected to electric pins in order to measure the current. The gold electrodes are deposited on a quartz substrate. The design of the electrodes is such that gold electrodes have an inter-electrode distance of 300 nm. Each substrate contains 40 pairs of electrodes, each pair of electrodes corresponds to one device. Figure 3.8 shows a picture of the interdigitated gold electrode substrate before QDs deposition and reports a schematic representation of the interdigitated electrodes and how they are connected to the signal-reading apparatus.
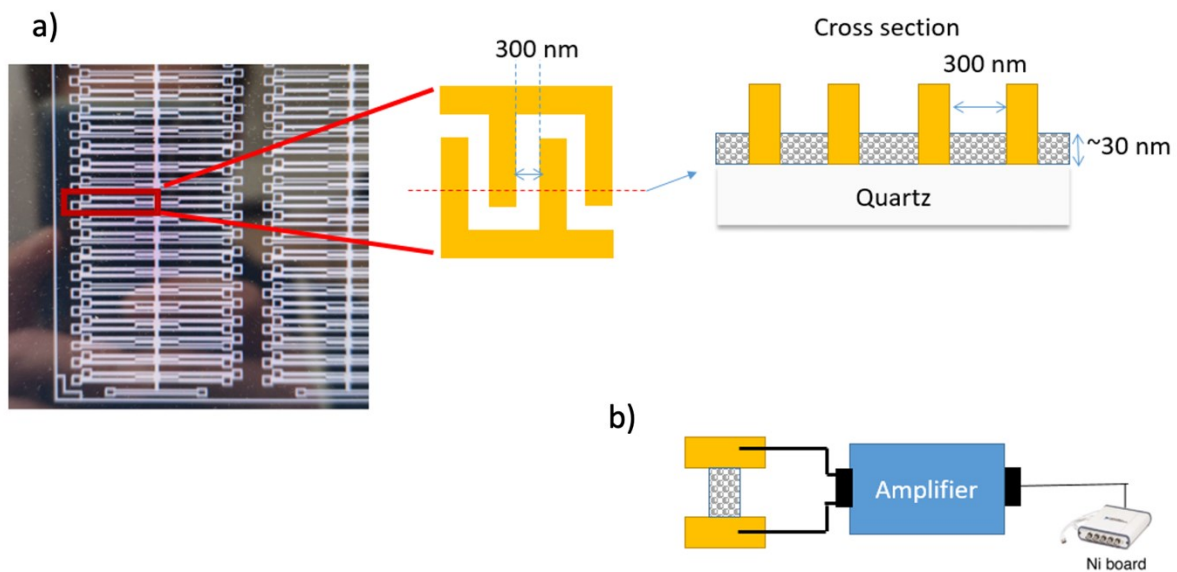
*Figure 3.8:* a) Substrate with interdigitated gold electrodes before QDs coating. The red rectangle pinpoints a single working device. Each sample contains 40 devices, divided into four columns. In addition, a pictorial representation of the gold interdigitated electrodes is shown. b) Connection between the gold electrodes and the signal-reading apparatus, composed of a transimpedance amplifier and a National Instrument board.
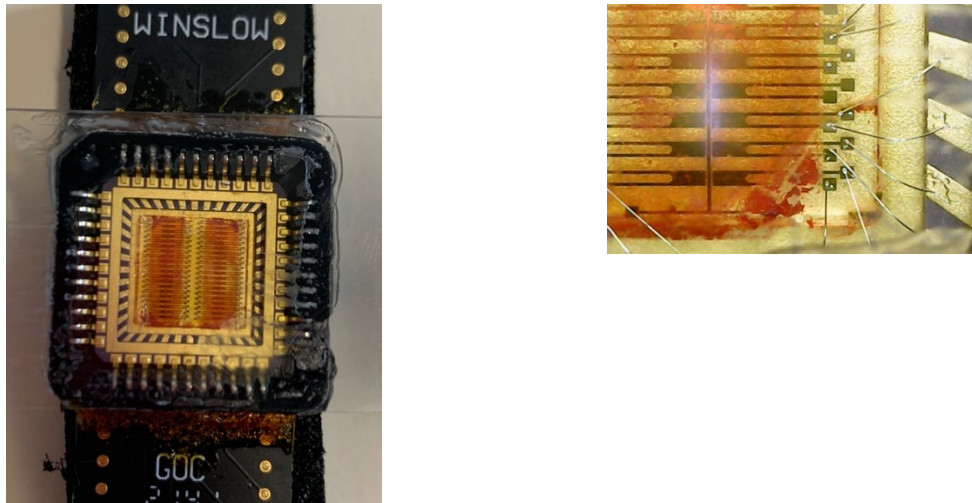
Figure 3.9: On the left is reported a photo of the chip in scale 1:1, whereas on the right a zoom on the wirings.

Figure 3.9 illustrates a real photo of the chip in scale 1:1 and a zoom on the wirings.

The synthesis of the QDs was performed following a procedure reported in the literature [53,54]. The synthesis procedure led to obtain CdSe QDs stabilized by octadecylamine ligands and dispersed in hexane. The mean diameter of the QDs and the size dispersion of the sample were verified by TEM (Figure 3.10). Overall, the QDs have a mean diameter of about 3.7 nm with a size dispersion of about 8%.
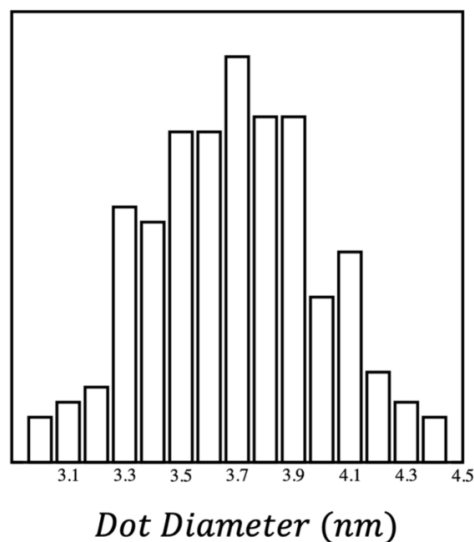
Figure 3.10: Size distribution of the QDs film obtained with TEM microscopy. The size dispersion amounts to 8%.

In order to promote inter-dot interactions and promote the formation of strongly coupled meso-structures (mainly dimers), covalent links between dots have been promoted using 1,3-propanedithiol (pDT), having a nominal length of 0.55 nm, following an approach already reported in the literature for dimer formation [45].

Briefly, a stock solution of pDT in ethanol with a suitable concentration was prepared. Then a cleaned interdigitated gold substrate (like the one shown in Figure 3.8) was immersed for 10 min in this solution to form a self-assembled monolayer of pDT on the gold to favor the ensuing adsorption of the QDs. 20uL of QD solution were then spinned onto this functionalized substrate at 1000 rpm for 30 s. Subsequently, the sample was immersed again in the pDT solution for the ligand exchange. These last two steps (QDs spinning and immersion in pDT solution) were repeated iteratively for 10 times, so to obtain a final QDs film with an optical density suitable for the 2DES experiments.

The resulting interdigitated gold substrate covered by a thin film of interacting QDs was then wired for electrical measurements and encapsulated. To prevent oxidation, all these procedures (from QDs deposition to encapsulation) were carried out under a dry nitrogen environment. The correct functioning of the final device was verified with I-V measurements. Typically, not all the 80 devices on each substrate were photoactive. Photocurrent-detected 2DES experiments were thus possible only on a limited number of devices.

Chapter 4
Experimental Set-up and Data Analysis

In this Chapter we will present a brief description of the experimental optical set-up we employed in this work. As already pointed out in Chapter 2, one of the main advantages of action-based 2DES experiments is the much simpler optical set up, which is a consequence of employing a fully collinear excitation scheme instead of a fully non-collinear one, like in the case of coherence-based 2DES. Figure 4.1 depicts the optical set-up employed in this work. A description of each of its components can be found in the following sections.
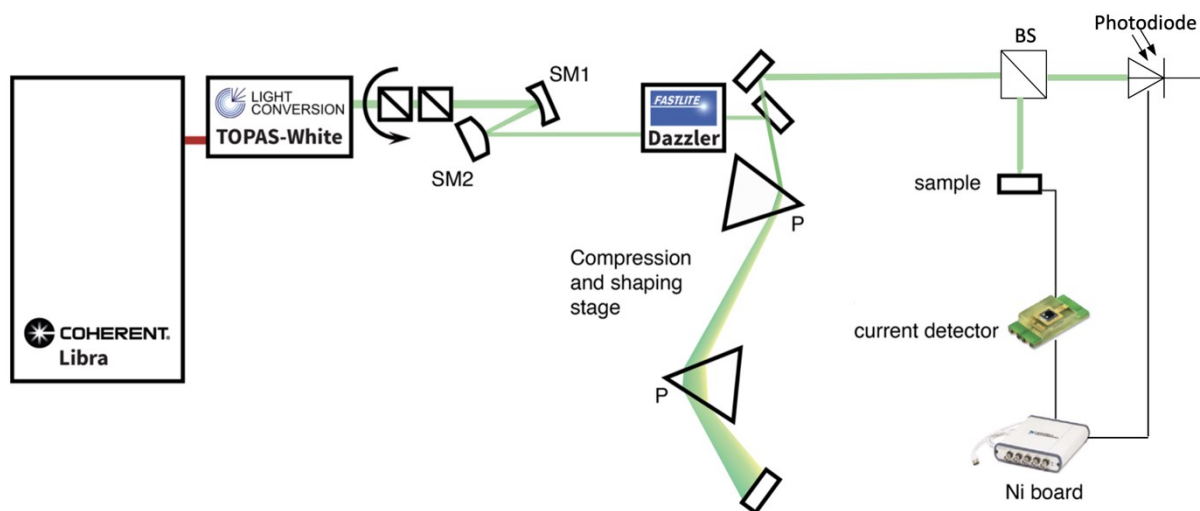
Figure. 4.1: *Optical set-up employed in fully collinear 2DES experiments. Abbreviations: (SM) spherical mirrors, (P) prism compressor, (BS) beam splitter.*

4.1 Laser Source

The beam source is a Coherent® Libra Ti:Sapphire amplified system, which includes three main components:

1. An integrated Ti:Sapphire laser (*Vitesse*) generates a series of pulses with a repetition rate of 80 MHz. Each pulse has a bandwidth of approximately 12 nm, a duration of 100 fs, and an energy of 3.5 nJ. The output of this laser represents the *seed*.

2. A Nd:YAG laser at 527 nm (*Evolution*) emits nanosecond pulses and it is employed in order to amplify the seed beam.

3. A regenerative optical amplifier (*Regen Cavity*) in which a second Ti:Sapphire rod, maintained in a condition of population inversion by the Evolution beam, is employed to amplify the seed pulses of the *Vitesse* up to 10^5 times. In a regenerative amplification, the seed beam is first stretched in time by a grating stretcher to preserve the Ti:Sapphire crystal. The amplified seed coming out is then compressed again by a grating compressor, restoring the initial pulse duration.

The Libra output consists of a train of pulses with a repetition rate of 3 kHz, where each pulse has a bandwidth of about 12 nm centred at 800 nm, with a duration of 100 fs and an energy of 0.8 mJ.

4.2 Non-collinear Optical Parametric Amplifier (NOPA)

A Light Conversion® Topas White, functioning as a non-collinear optical parametric amplifier (NOPA), is employed to tune the 800 nm wavelength of the laser into a broad spectrum, ranging from 540 to 780 nm.

Prior to entering the TOPAS White, the pump beam (output from the Libra) passes through a beam stabilizer device (Newport® Guide Star II), consisting of two piezoelectric mirrors and two cameras. This device compensates for any spatial deviations in Libra's output over time, ensuring the stability of the optimal alignment throughout the experiment.

In the TOPAS, the incoming light is divided into two beams, with 1% focused on a sapphire plate that generates supercontinuous white light through nonlinear processes. The white light is then collimated using spherical mirrors and directed into a pulse shaper, in order to modify the chirp and to regulate the final amplified beam's bandwidth. The remaining 99% of the input beam passes through a beta-barium-borate (BBO) crystal, resulting in the generation of a second harmonic beam at 400 nm. This beam is further split into two portions, with 5% serving as the preamplification beam and the remaining 95% as the primary amplification beam.

The white light and the 400 nm amplification pulses interact within a second BBO crystal. The amplification of specific spectral components of the white light (i.e., the selection of the wavelength of the output beam) is achieved by rotating the crystal and adjusting the incident angle between the three interacting pulses to maximize the output beam intensity (according to specific phase matching relationships). In order to achieve this, the precise overlap of the three pulses in both spatial and temporal domains is mandatory. The resulting pulse output has a duration of approximately 10 fs and an energy ranging from 1 to 30 μJ.

The laser spectrum is then assessed using an Avantes® fiberoptic spectrometer.

4.3 Pulse Compressing and Shaping Methods

In ultrafast spectroscopy, the control over the phase and the amplitude of ultrafast laser pulses is of fundamental importance. In fact, the output of the TOPAS is a broadband pulse that can experience a phenomenon known as "temporal chirp". When a pulse is chirped, it means that the different components of this pulse, i.e. the different colours, travel with different velocities, thus affecting the pulse duration and, in turn, the shape of the optical responses [55-57].

Since this is a crucial aspect in multidimensional spectroscopies, this section will provide some insightful information about how the phase affects the shapes of ultrashort pulses.

Let's consider the case of a linearly polarized electric field, propagating in time, that can be described as follows [58]:

$$E(t) = A(t)\cos\left(\Phi(t)\right) \tag{4.1}$$

Where:

- $A(t)$ is the *envelope function,*
- $\Phi(t)$ is the total phase, expressed as $\Phi(t) = \omega_0 t + \varphi(t)$.

This total phase $\Phi(t)$ is a function of the central frequency ω_0 and of the time-dependent phase, which is, in turn, expressed by the following Taylor's series in the time domain:

$$\varphi(t) = \sum_{n=0}^{\infty} \frac{\varphi_n}{n!} t^n = \varphi_0 + \varphi_1 \frac{t}{1!} + \varphi_2 \frac{t^2}{2!} + \varphi_3 \frac{t^3}{3!} + \cdots \tag{4.2}$$

Where φ_n are the phase coefficients, defined as:

$$\varphi_n = \frac{\partial^n \varphi(t)}{\partial t^n} \tag{4.3}$$

According to this series, if the phase terms with $n \geq 2$ are nonzero, the pulse experiences a temporal broadening. When this happens, the bandwidth limit $\tau_G \Delta\omega$ (which describes the relationship between the shortest possible Gaussian pulse duration τ_G and the spectral full width at half maximum (FWHM) $\Delta\omega$ [10]), is exceeded.

An analogous expression for the phase in the frequency domain can be obtained as a Taylor expansion around the carrier frequency of the pulse:

$$\varphi(\omega) = \sum_{m=0}^{\infty} \frac{\varphi_m(\omega_0)}{m!} (\Delta\omega)^m \tag{4.4}$$

$$= \varphi_0 + \frac{1}{1!}\varphi_1(\Delta\omega) + \frac{1}{2!}\varphi_2(\Delta\omega)^2 + \frac{1}{3!}\varphi_3(\Delta\omega)^3 + \cdots$$

Where:

- The coefficients are defined as: $\varphi_m = \frac{\partial^m \varphi(\omega)}{\partial\omega^m}$,

- $\Delta\omega = \omega - \omega_0$.

The first and second terms of this expansion do not affect the shape of the pulse, whereas the third term, i.e. the second order phase term $\frac{1}{2!}\varphi_2(\Delta\omega)^2$, called "group delay dispersion" or GDD, introduces a frequency-dependent delay of the different components of the pulse. Therefore, GDD is responsible for a *chirp* that stretches the pulse in the time domain, meaning that the different components of the pulse, i.e. the different colours, travel with different velocities.

Since this temporal chirp deeply affects the shape of the pulse and therefore the outcome of the experiment, it must be corrected. To this aim, in our setup we made use of a pulse-shaper and a prism compressor.

### 4.3.1 Pulse Shaper Compression

The first compression stage of the laser pulses was performed by employing an *acousto-optic programmable dispersive filter* (AOPDF, Fastlite® *Dazzler*). As we already mentioned, this

instrument is employed as a pulse shaper, and we will now present a brief description of its operating mechanism.

An AOPDF is a kind of acousto-optic modulator (AOM) that relies on the interaction between a polychromatic acoustic wave and polychromatic optical wave in a birefringent crystal with acousto-optic properties, such as a paratellurite crystal TeO_2 [59]. If the correct phase-matching conditions are met:

$$\begin{cases} \mathbf{k}_{diff}(\omega_{opt,diff}) = \mathbf{k}_{in}(\omega_{opt,in}) + \mathbf{k}_{ac}(\omega_{ac}) \\ \omega_{opt,diff} = \omega_{opt,in} + \omega_{ac} \end{cases} \qquad (4.5)$$

the interaction between the acoustic and the optical waves generates a new optical beam, the *diffracted* beam, which is characterized by a diffraction angle of 1° with respect to the input optical axis. This acousto-optic effect results in a change of the refractive index of the material. In the *Dazzler*, (Figure 4.2) a transducer triggered by a time-dependent radiofrequency (RF) electronic signal, induces the propagation of an acoustic wave. This wave travels with a velocity v along the z-axis, spatially reproducing the temporal shape of the RF signal [59].
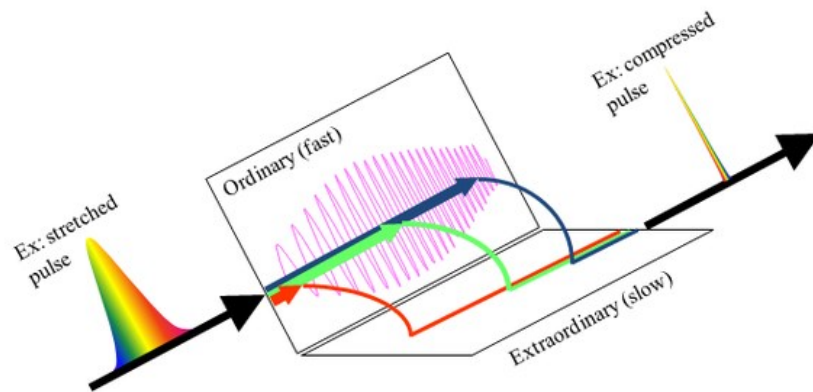
Figure 4.2: Pictorial representation of the working principle of the Dazzler in terms of the group delay control. Picture adapted from [58].

The incoming optical pulse is *ordinary* polarized. Once it enters the acousto-optic crystal, each optical frequency ω travels a specific distance until it reaches a spatial frequency in the acoustic grating that is phase-matched. At this specific position $z(\omega)$, a portion of the energy that undergoes diffraction results in the generation of an *extraordinary* polarized component. Upon reaching the crystal output, the diffracted pulse comprises all the spectral components that experienced diffraction at different positions.

Due to the different group velocities associated with the ordinary and extraordinary polarizations, each frequency experiences a different group delay. The group delay $\tau(\omega)$ applied to the diffracted pulse, can be expressed as [59]:

$$\tau(\omega) = \frac{n_{g_o}(\omega)}{c \cdot z(\omega)} + \frac{n_{g_e}(\omega)}{c \cdot (L - z(\omega))}$$ (4.6)

Where:

- $n_{g_o}(\omega)$ and $n_{g_e}(\omega)$ are the ordinary and extraordinary group indexes along the propagation direction,
- L is the length of the crystal.

By carefully regulating the position $z(\omega)$ where the diffraction takes place, it becomes possible to control the group delay of the pulse. The amplitude of the resulting output pulse is controlled by the acoustic power at this position.

4.3.2 Prism Compression

Since the paratellurite crystal introduces a positive GDD on the input laser pulse, this delay can be compensated by introducing a negative GDD by employing a prism compressor or a grating compressor. In the optical set-up employed in this work, the static compression is achieved by the action of two optical prisms. The first prism disperses the input beam in all its spectral components, whereas the second prism collimates them.

By adjusting the distance between the prisms and their relative angle, it becomes possible to manipulate the optical chirp, by controlling the sign and the amount of introduced dispersion. Consequently, this allows the regulation over the time delay and phase shifts among the various spectral components.

4.4 Phase Modulation

In Chapter 2, the importance of the phase-sensitive detection in action-based 2DES approaches was pointed out. In this context, in fact, the different contributions to the signal (e.g. the

rephasing and non-rephasing contributions) can be separated by employing different phase-selection schemes, which allows us to extract the different contributions to the signal according to their phase rather than their spatial direction. To fulfill this goal, we employed the *Dazzler* not only as a pulse shaper but also as the core instrument for the phase modulation step [9,60,61]. In fact, the waveform of the *Dazzler* is programmed to generate for each incoming pulse a sequence of four exciting pulses, separated in time by specific time delays and characterized by a specific phase (Figure 4.3).
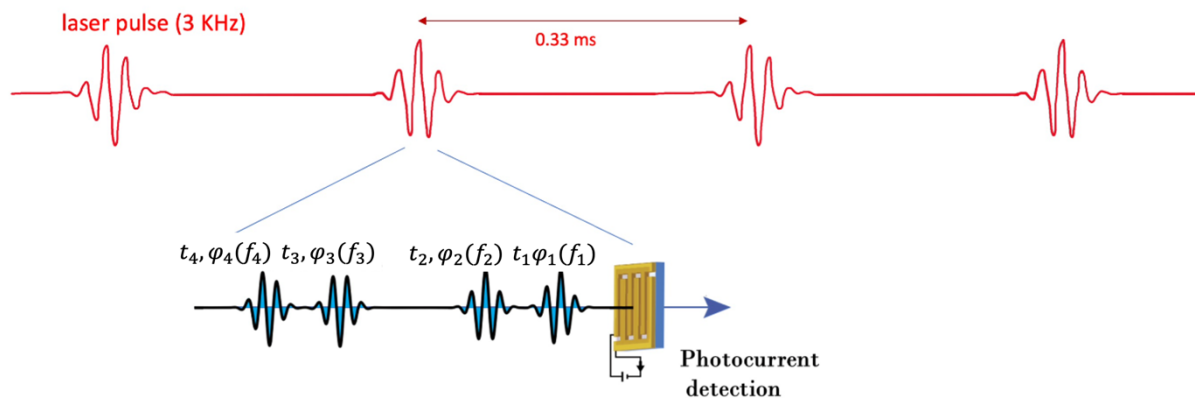
Figure 4.3: *Pulse-by-pulse phase modulation scheme. The incoming laser pulses from the TOPAS are shaped by the Dazzler into four different pulses separated by specific time delays t_1, t_2, t_3 and with specific phases (φ_1, φ_2, φ_3, φ_4) that are modulated with frequencies f_1, f_2, f_3 and f_4 (Chapter 2, Section 2.2.1).*

The phase modulation scheme we employed in this work was carefully designed keeping in mind some restrictions of our experimental 2DES set-up [9]:

1. The first limit is the fast memory of the *Dazzler*. In fact, in order to ensure a consistent modulation frequency, it is mandatory to employ pulse-by-pulse shaping. While the FIFO (first in, first out) memory of the *Dazzler* facilitates this process, it has restricted storage capacity, accommodating only up to 80-90 waveforms. Nevertheless, this sequence of waveforms can be endlessly reiterated without interruption.

2. The second limit is that the four frequencies f_i that modulate the phases of the exciting pulses (and therefore the final signal) must be chosen so to start and finish the modulation patterns with the same phase.

Because of these two restrictions, we chose a pattern of 72 waveforms. We then decided to keep constant the phase of the first exciting pulse, while the other three pulses increase their phase of $\pi/6$, $\pi/8$, and $\pi/9$ at each laser pulse. They all start with phase $\varphi_i = 0$ and at the

72nd laser pulse they will have phases equal to $\varphi_2 = 2\pi - \pi/6$, $\varphi_3 = 2\pi - \pi/8$ and $\varphi_4 = 2\pi - \pi/9$, respectively. At the next laser pulse, (i.e., at the 73rd waveform, corresponding to the first one of the next sequence), the phase will be $2\pi = 0$ for each pulse and the following sequence will start. We chose to repeat this sequence 42 times in order to complete each pattern in approximately one second: $72 \times 42 = 3024$. Considering this repetition rate, the final modulation frequencies f_i were chosen as:

$$f_1 = 0, \qquad f_2 = \frac{3024}{72} \cdot 6 = 252 \ Hz,$$

$$f_3 = \frac{3024}{72} \cdot 8 = 336 \ Hz, \qquad f_4 = \frac{3024}{72} \cdot 9 = 378 \ Hz.$$

In order to extract the fourth order signal (Chapter 2), we filter out the signal at the desired phase combination For the rephasing signal the phase combination is $-\varphi_1 + \varphi_2 + \varphi_3 - \varphi_4$, and the rephasing signal, considering the laser repetition rate of $3 \ kHz$, will be modulated at the frequency: $f_{s,rephasing} = 3000 - f_1 + f_2 + f_3 - f_4 = 3210 \ Hz$. Instead, for the non-rephasing signal the phase combination is: $+\varphi_1 - \varphi_2 + \varphi_3 - \varphi_4$, and the non-rephasing signal, considering the laser repetition rate of $3 \ kHz$, will be modulated at the frequency: $f_{s,non-rephasing} = 3000 + f_1 - f_2 + f_3 - f_4 = 2706 \ Hz$. In general, imposing $f_1 = 0$ could represent an issue since both negative and positive contributions could be generated at the same frequency. However, since the undesired contribution path is a coherence, it will not contribute to the excited-state population and thus its contribution to the read out signal will be zero. The selection of divisors such as 6, 8, and 9 was proven to be particularly suitable as it ensures that the linear and fourth order components can be found at distinct frequencies.

4.5 Signal Detection

The detection scheme is composed as follows: a beam splitter is positioned after the prism compressor, in order to split the incident beam into two different beams. One beam is focused on the sample, which is connected via a BNC cable to a National Instrument ADC (NI Usb-4432) board (Figure 4.1). The board is connected to a computer that acquires the data. In addition, the sample is connected to a transimpedance amplifier, which is a current-to-voltage

converter, employed in the setup to amplify the current signal generated by the sample and convert it into a voltage. The second beam is, instead, sent to a Silicon photodiode, which is employed as a reference in order to eliminate the nonlinear artifact originating from the *Dazzler*, as described in the next section.

The signal detection process is summarized in Figure 4.4. After a sequence of four delayed and phase-modulated pulses reaches the sample, a current/voltage signal is generated and is read out by the National Instruments card. This allows the retrieval of the raw signal, measured in volts as a function of time. This raw signal in time contains all the different signal contributions (linear, nonlinear, rephasing, non-rephasing, etc.), each one modulated at a specific combination of the modulation frequencies f_i, as described in Chapter 2, Section 2.2.

This signal is then Fourier-transformed, to obtain the so-called phase-modulation spectrum, where the different signal components appear at different frequencies. For example, following what is explained in Section 4.4, one can expect to find the rephasing fourth order signal at a frequency of $3210 \, Hz$, and the non-rephasing signal at a frequency of $2706 \, Hz$. By following the evolution of the various components in the phase-modulation spectrum as a function of the delay-times (t_1, t_2, t_3), a set of temporal data $S(t_1, t_2, t_3)$ is collected and, by taking the Fourier transform along suitable axes, the corresponding 2D response is retrieved, where the signal is expressed as a function of ω_1, t_2, ω_3.
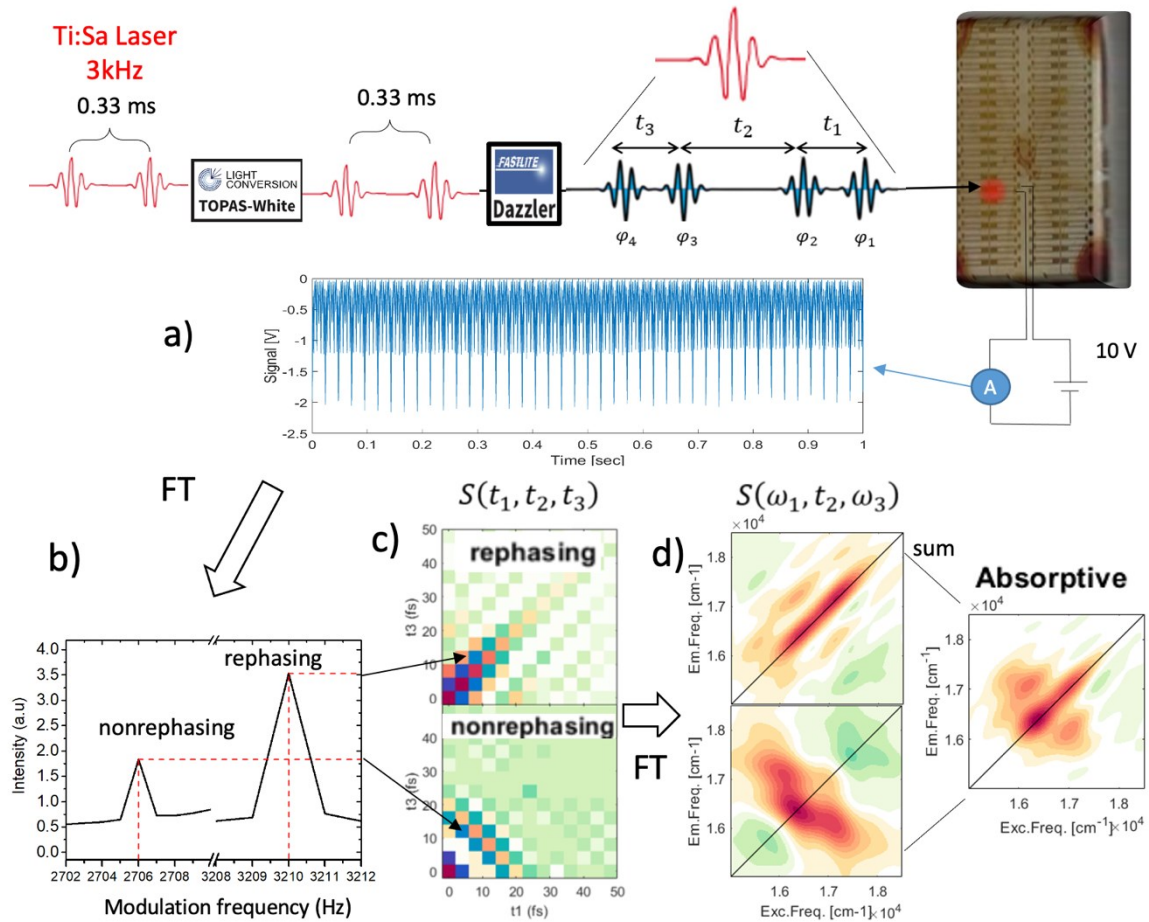
Figure 4.4*: Schematic representation of the working principle of PC-2DES. a) The photo-conductive device, after the interaction with a sequence of four phase-modulated laser pulses shaped by the Dazzler, emits an incoherent signal (i.e. a photocurrent). This incoherent signal is recorded as a raw signal, expressed as a function of time. b) By taking the Fourier transform of this raw signal, the phase-modulation spectrum is obtained, which contains the various contributions to the optical response, each one appearing at a well-defined combination of the phase-modulation frequencies f_i. c) The 2DES maps are rebuilt by extracting the components at all time-delays. d) After the data processing and Fourier transform along t_1 and t_3 , the rephasing (signal modulated at $3210\,Hz$) and non-rephasing (signal modulated at $2706\,Hz$) maps as a function of ω_1, t_2, ω_3 are obtained and the sum of these gives the absorptive maps.*

4.6 Controlling the Acousto-Optic Nonlinearity

An important step of this work regarded the calibration of the *Dazzler* in order to account for the intrinsic nonlinearity of the acousto-optic interaction, becoming non-negligible at large acoustic powers ($A_0 > 20\%$) [10]. This nonlinearity causes the laser output from the *Dazzler* to scale sub-linearly as a function of the applied acoustic power (Figure 4.5) and must be corrected in order to properly visualize and interpret the weak signal coming from the sample.

In fact, this nonlinear subscaling gives rise to a characteristic artifact in the 2DES maps, which is manifested as a marked diagonal line across the map (Figure 4.5).
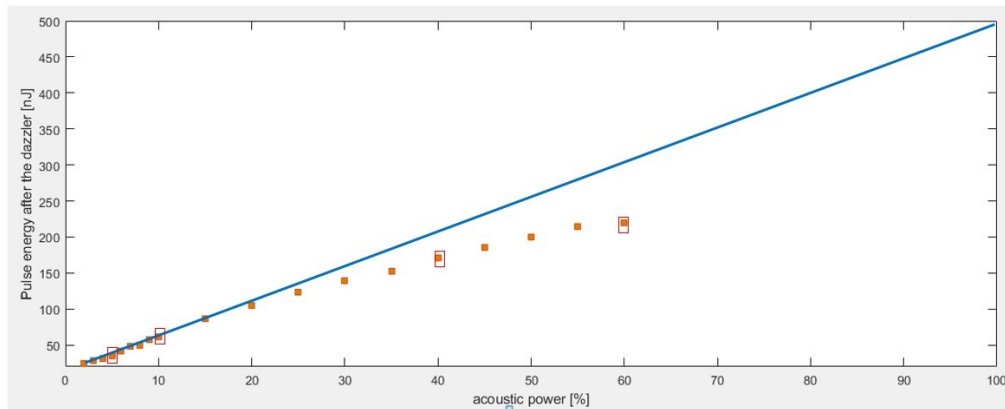

Figure 4.5: *Measured laser power (orange dots) as a function of the applied acoustic power A_0. It is evident that the linear relation between the acoustic amplitude and the shaped optical power only holds for small acoustic amplitudes and becomes nonlinear at large shaping efficiencies. Therefore, it must be corrected by performing a calibration procedure.*

The presence of this artifact was recognized only recently, and it was soon realized that removing its contribution from the real signal is a very challenging task. This has hindered the diffusion of action-based 2DES setups based on *Dazzler* pulse shapers and explains why only a limited number of papers on the topic have been published so far.

The simplest way of avoiding the artifact would be to acquire the sample signal in the linear regime, i.e., setting up an acoustic power <1%. In these conditions, however, the majority of the systems do not show any signal because the exciting beam intensity is too low to promote any nonlinear optical response. Therefore, to measure a meaningful signal from the sample, higher acoustic powers are needed, falling necessarily in the nonlinear regime.

Therefore, in order to account for this nonlinear subscaling of the laser power as a function of the acoustic power, we have developed a home-built calibration procedure, inspired to the pioneering work of Sebastian Röding [10], which is summarized in Figure 4.6.
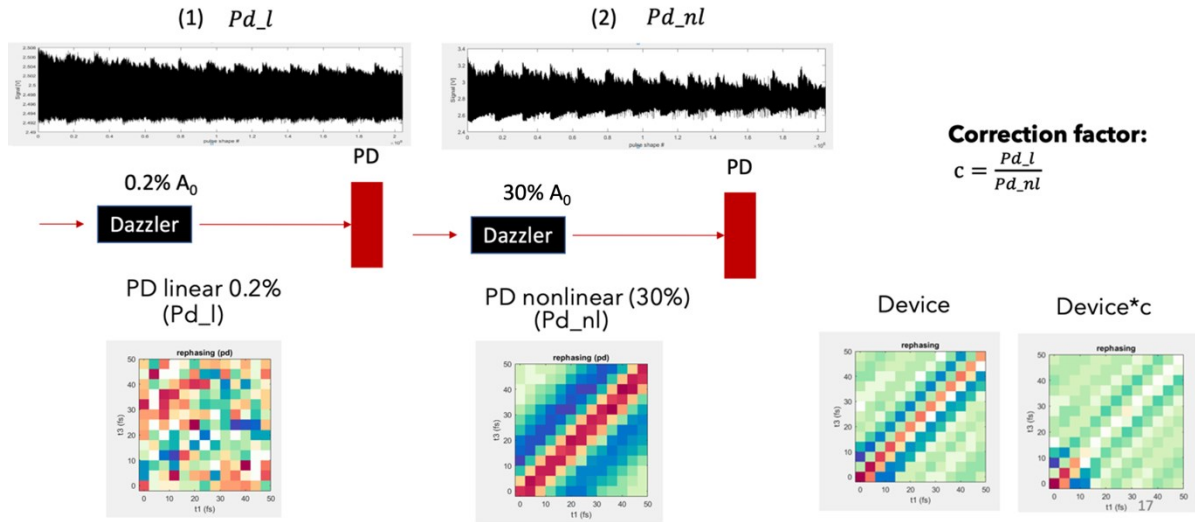
Figure 4.6: Dazzler's artifact correction procedure. In the upper panels the raw signal measured as a function of the pulse shape is depicted for the linear (left panel) and nonlinear (right panel) regimes. The lower panels represent the time domain rephasing contributions, for the reference photodiode PD (left panels) and for the sample (right panels).

The calibration procedure was carried out as follows:

1. By using a simple Silicon photodiode as a photodetector, the shaped output laser power was first measured in the *linear* range ($A_0 = 0.2\%$), yielding to the signal labelled as Pd_l;

2. The same measurement was performed in the nonlinear regime ($A_0 = 30\%$), thus obtaining Pd_nl.

3. According to these measurements, we obtained the correction factor C for each individual pulse shape, defined as:

$$C = \frac{Pd\_l}{Pd\_nl} \tag{4.7}$$

4. The signal of the sample was then measured in the nonlinear regime of the acoustic power (Sig_{device}), thus obtaining a bidimensional map displayed in the time domain that featured an intense diagonal line, i.e. the nonlinear artifact.

5. The raw signal of the device Sig_{device} was then corrected by applying the correction factor, according to:

$$Sig_{corr} = C \cdot Sig_{device} \tag{4.8}$$

The calibration procedure has proven to be effective as we were able to eliminate the majority of the artifact, as shown in Figure 4.6 (bottom panels).

4.7 Intensity Autocorrelation of the Ultrashort Laser Pulse

The correct interpretation of the results of any ultrafast technique, requires the careful characterisation of the exciting pulse duration. To this aim, we employed an *intensity autocorrelation* method, which involves splitting the pulse into two, variably delaying one with respect to the other, and overlapping them in a fast-responding second harmonic generation nonlinear crystal. In our setup, we employed a BBO crystal, the *Dazzler* to split the pulse and delay the two resulting beams, and an optical fiber photodetector.

In an autocorrelation experiment, the *Dazzler* waveform was programmed in order to split the incoming pulse into two identical replicas and delay one replica in time with respect to the other. Only when the two pulses are temporally overlapping, the conditions to generate the second harmonic beam are met. Consequently, the overlapping beams interfere with each other, and the intensity of the resulting second harmonic signal depends on the temporal overlap between the pulses.

The second harmonic signal after the BBO crystal is measured by the optical fiber as:

$$E_{sig}^{SHG}(t,\tau) \propto E(t)E(t-\tau) \tag{4.9}$$

Where τ is the temporal delay between the two beam's replicas.

The intensity associated with this field is proportional to the product of the intensities of the two input pulses:

$$I_{sig}^{SHG}(t,\tau) \propto I(t)I(t-\tau) \tag{4.10}$$

Since the detection time of the typical optical detectors is too slow to capture this signal, they will measure the second-order autocorrelation $A^{(2)}(\tau)$:

$$A^{(2)}(\tau) = \int_{-\infty}^{\infty} I(t)I(t-\tau)dt \tag{4.11}$$

Assuming that the pulse has a Gaussian shape, also this autocorrelation curve will have a Gaussian shape. The pulse duration can thus be obtained dividing the FWHM of the autocorrelation by $\sqrt{2}$ [62].

4.8 Data Analysis

The information obtained from 2DES experiments is examined and interpreted through a specific home-made procedure implemented with the MATLAB® R2023b software.

The output of a 2DES experiment is a three-dimensional matrix of data that is obtained by scanning the values of the time delays t_1, t_2, t_3 between the laser pulses. In order to analyze this 3D-matrix various techniques can be employed [63-66]. In our research group, we have introduced a *multi-exponential global fitting model* for this purpose, whose detailed description can be found in ref. [67].

The fitting function, defined as:

$$f = \sum_{n=1}^{N} a_n e^{i\varphi_n} e^{-\frac{t_2}{\tau_n}} e^{-i\omega_n t_2} \tag{4.12}$$

is employed to simultaneously fit the signal decay at each coordinate of the 2DES maps.

This approach is particularly advantageous since it involves fewer operations compared to alternative analysis methods, allowing simultaneous access to both oscillating ($\omega_n \neq 0$) and non-oscillating ($\omega_n = 0$) components. This analysis is performed in a single step without the need for any preliminary subtraction procedure. Each component, labeled with the subscript n, is associated with a specific kinetic constant τ_n. The fitting process yields two different kinds of amplitude maps a_n, referred to as "decay-associated spectra (DAS)" when $\omega_n = 0$, and "coherence-associated spectra (CAS)" when $\omega_n \neq 0$.

The DAS are associated with non-oscillating exponential components. The real part of a DAS provides information about the evolution of the population along t_2, indicating whether the signal is rising or decaying in time. Indeed, the DAS maps show positive peaks when the signal undergoes exponential decay, whereas they show negative peaks when the signal is increasing.

The CAS are analogous to DAS, but they refer to oscillating contributions of the signal, described with complex exponential functions. They are useful in order to characterize a particular beating mode in terms of its frequency ω_n, amplitude a_n and phase φ_n.
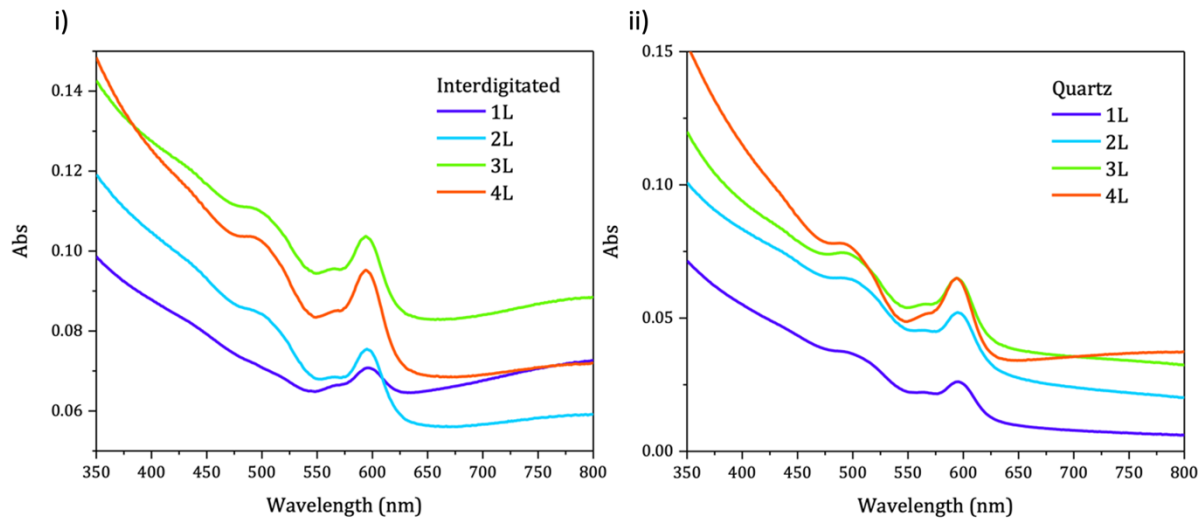
Chapter 5
Results and Discussion

In this final Chapter, we will present the results of the preliminary experimental characterization of the QDs-based device by means of photocurrent detected 2DES.
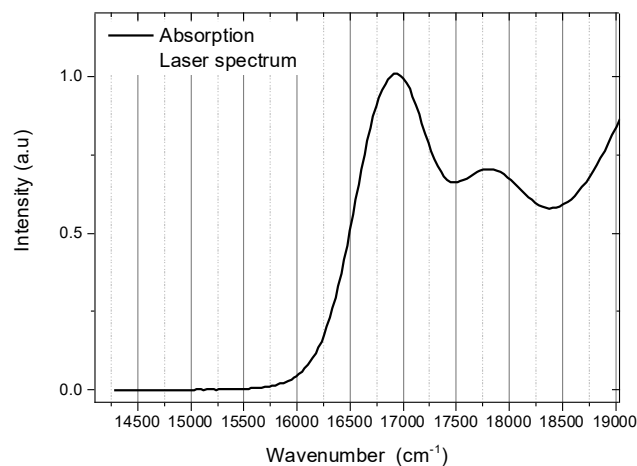
5.1 Absorption Spectroscopy

The characterization of the sample by linear absorption spectroscopy is a necessary step to be performed before the 2DES measurements. Absorption spectroscopy relates the amount of light absorbed by a sample to the wavelength of the incident radiation. Usually, it is exploited to evaluate the sample's concentration or molar extinction coefficients (or cross section) by applying the Lambert-Beer law. In our case, the absorption spectra are essential to identify the main electronic transitions that are involved in the spectral region addressed by the exciting laser pulse in 2DES measurements. The sample devices prepared for the PC-2DES experiments (Chapter 3, Section 3.4), are assembled on an opaque support, which do not allow the measurements of the absorption spectra in the typical transmissive configuration. Therefore, our collaborators prepared replicas of the same devices by depositing QDs (i) on interdigitated gold electrodes on a transparent quartz substrate and (ii) on a simple quartz slide without electrodes. They measured the absorption spectra of these samples after each QDs layer deposition. The obtained spectra are reported in Figure 5.1

i)

ii)

The absorption spectra on both substrates show very similar features, which confirms that the presence of gold electrodes underneath the QD layers does not affect their optical properties. In both cases, two main peaks could be identified: a maximum absorption peak located at 594 nm (= 16835 cm^{-1}), which corresponds to the first excited state, and a weaker peak at 560 nm (=17850 cm^{-1}), which we attributed to the second excited state.

5.2 PC-2DES measurements

Figure 5.2: *Normalized absorption spectrum of the QDs film deposited onto the interdigitated gold electrodes (black line). The red area represents the spectral profile of the laser used for the PC-2DES measurements.*

When performing 2DES measurements, the ideal condition would be to excite the sample with a very broad laser spectrum, to excite with the same intensity the highest possible number of transitions. Unfortunately, this is often not possible due to technical limitations that limit the achievable spectral bandwidth of the exciting pulses. Figure 5.2 compares the absorption spectrum of our samples with the spectral profile of the pulse used in the PC-2DES experiment. The laser covers the lower energy transition and only partially the higher energy transition. It was not possible to push the laser spectrum further to the blue to fully cover also the higher energy transition because of the intrinsic bandwidth limitations of the NOPA. However, even if the experimental conditions were not optimal, we still succeeded in measuring our sample, exciting both the main transitions appearing in the absorption spectrum. A similar experimental configuration was proved to be successful also in previous coherence-based 2DES experiments on similar samples [44,45,51].

A first qualitative analysis of the results can be performed by looking at the evolution of the signal in the 2DES maps as a function of the population time t_2. Figures 5.3 and 5.4 represent PC-2DES maps at selected values of t_2 in the range 0-50 fs and 100-400 fs, respectively. These maps were collected by scanning t_1 and t_3 from 0 to 48 fs in steps of 4 fs, and t_2 from 0 to 400 fs in steps of 7 fs.
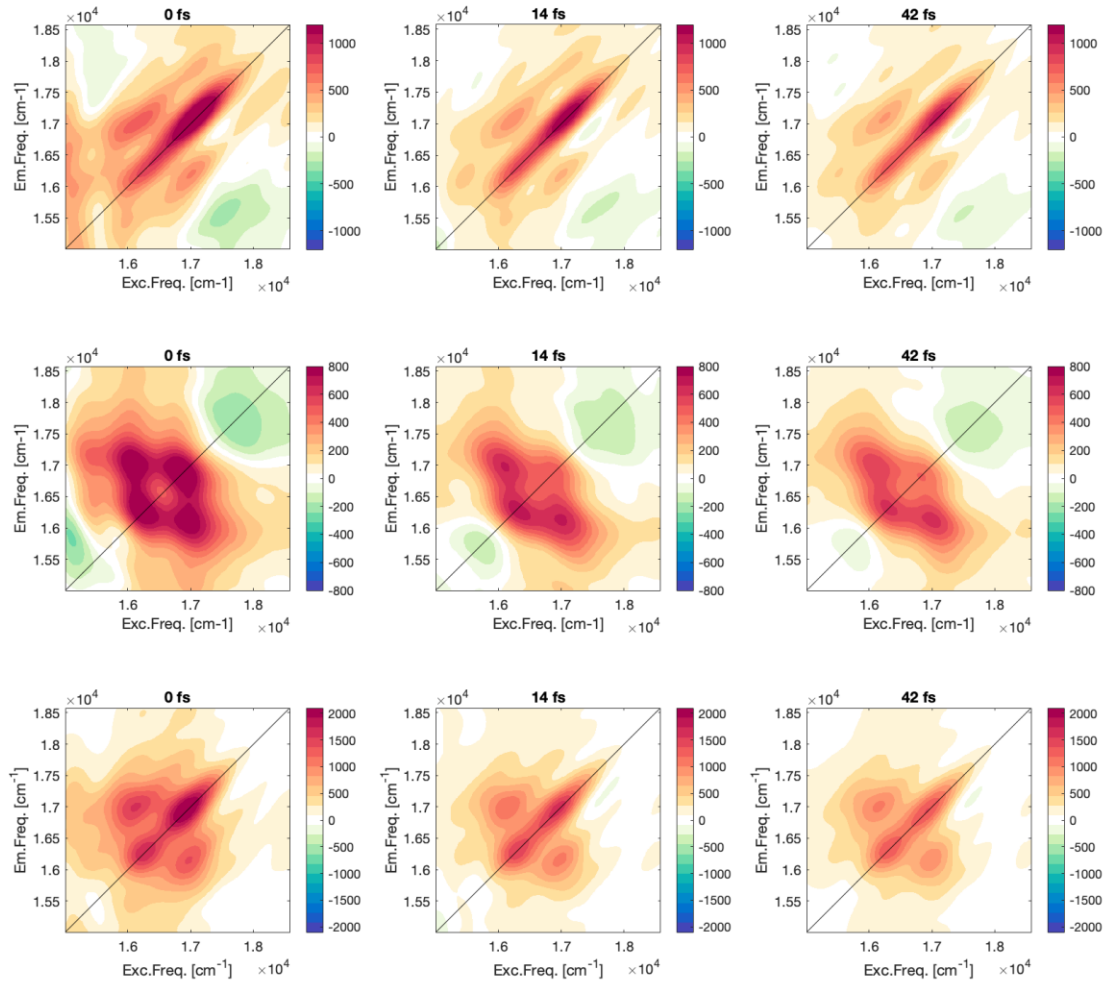
Figure 5.3*: PC-2DES maps for the rephasing (upper panel), non-rephasing (central panel) and absorptive contribution (lower panel) evaluated at short t_2 times. The intensity of the signal was normalized with respect to the map at 0 fs.*
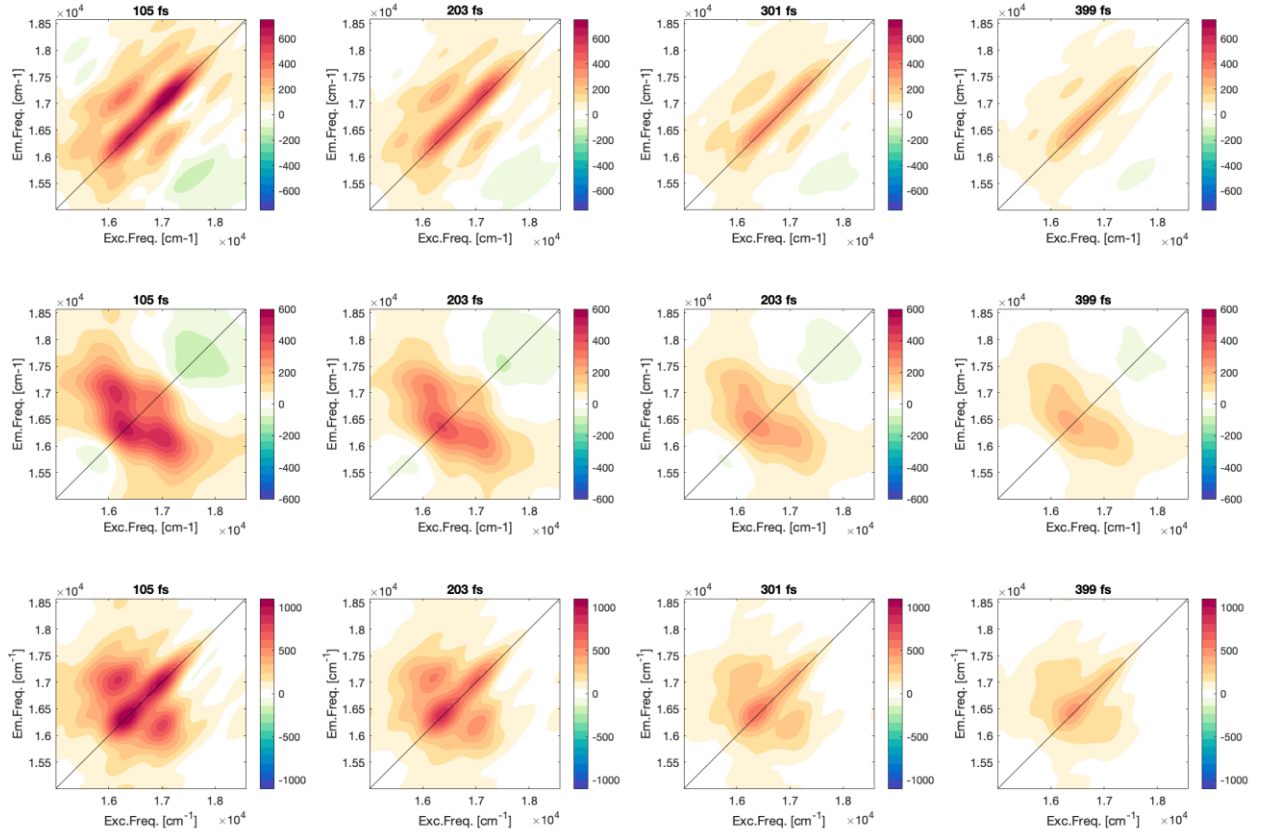
Figure 5.4: *PC-2DES maps for the rephasing (upper panel), non-rephasing (central panel) and absorptive contribution (lower panel) evaluated at long t_2 times. The intensity of the signal was normalized with respect to the map recorded at 105 fs.*

The maps show two clearly distinguishable peaks on the diagonal, which, due to the size distribution of the sample, are elongated along the diagonal direction in the case of the rephasing maps, and along the anti-diagonal in the case of the non-rephasing maps. The elongation of the diagonal peaks is a well-known phenomenon in 2DES, as we already discussed in Chapter 2. This effect is due to *inhomogeneous broadening* and depends on the amplitude of the size distribution of the sample: the greater the size distribution, the more elongated the signal peak. Another important feature in the maps is the presence of cross-peaks, recorded already at very short population times. In general, in 2DES the presence of cross peaks is direct evidence of interaction between different electronic states (Chapter 2, Section 2.1). However, in the case of action-based 2DES, the origin of these spectral features is still under investigation. Currently, many works regarding this matter have been published, ascribing the presence of cross peaks mostly to exciton-exciton annihilation phenomena [16] or to excitonic

delocalization [68]. Several efforts, both from the experimental and theoretical side are currently being made in the multidimensional spectroscopy community to reach an agreement on the possible interpretation of these signals [69]. We are confident that our data on QDs will provide an important contribution to this discussion.

After this first qualitative description of the main features appearing in the PC-2DES maps, it is worth discussing in more detail their possible origin. For simplicity, let's focus our attention on the 2DES map registered at a population time of 203 fs, presented in Figure 5.5a. The panel above the map reproduces the linear absorption spectrum of the sample (black curve) overlapped with the laser spectral profile (red curve), as it was shown in Figure 5.2.
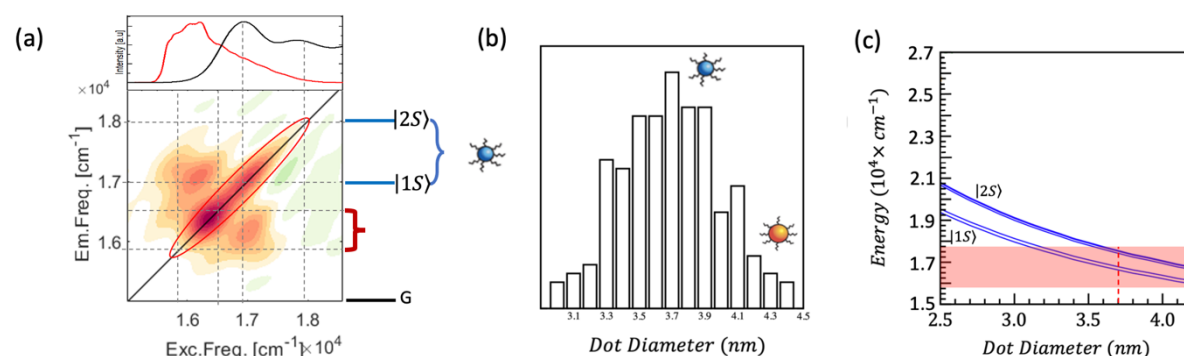
Figure 5.5*: a) 2DES map registered at a population time of 203 fs. b) Size distribution of the different QDs, measured by TEM microscopy. c) Theoretical simulation of the $|1S\rangle$ and $|2S\rangle$ energy levels in a monomer of QDs as a function of their average diameter. The red area represents the energy interval covered by the spectrum of the laser. The energy gap decreases with the diameter. The values at diameter of 3.7nm and at the biggest diameter 4.4nm correlates exactly with the energy levels shown in our PC-2DES map.*

As discussed before, two different peaks can be distinguished along the diagonal. The first one is located at 16835 cm^{-1}, which agrees with the frequency of the first excited state identified in the absorption spectrum. A second maximum is observed at lower energies, close to the intensity peak of the exciting laser profile (16250 cm^{-1}). It is well known that the signal recorded in a 2D map is the convolution between the optical response of the system and the exciting profile [1,3,70]. Therefore, it is reasonable to think that this signal is due to the enhancement of "red" states promoted by the convolution with the laser profile.

Now the question becomes: what is the nature of these red states?

The first hypothesis is that these red states are due to the fraction of QDs that in our inhomogeneous sample have bigger size and therefore lower energy gap. Figure 5.5b shows the size distribution in our QDs sample as determined by TEM analysis. The size distribution show that the dots have an average diameter of about 3.7 nm, but a non-negligible fraction of dots with diameters up to 4.4 nm are also present. According to theoretical simulations[6] (Figure 5.5c), the lowest energy transition for these bigger dots should fall exactly at the frequency of the lower diagonal peak. In this hypothesis, therefore, the peak at 16250 cm^{-1} should be ascribed to a specific fraction of quantum dots, characterized by a diameter of about 4.4 nm, whose signal is enhanced because of the peculiar spectral profile of the exciting beam.

One should also take into account that, as described in Chapter 3, Section 3.4, the sample device is prepared by deposition of different layers of QDs interspersed with layers of pDT, a bi-functional ligand that likely promotes the formation of dimers or higher order aggregates, as already demonstrated in our previous works [44,45,51]. As already mentioned in Chapter 3, Section 3.3, the dimer formation promotes the generation of new delocalized eigenstates, some of which are characterized by red-shifted energy. Therefore, also the promotion of inter-dot interactions could contribute to the recorded red signal.

In addition to this already complicated picture, one should also add the possible presence of Stark effects (i.e. the shifting and splitting of spectral transitions due to the presence of an external electric field), which can become relevant when a photocurrent is measured [71,72].

Another possible hypothesis is that these red states are trap states. It is indeed well-known that thiol ligands can modify the dot's surface creating defects of Se vacancies. These traps are usually located within the bandgap giving rise to red shifted features in absorption and emission spectra [73]. However, previous ultrafast measurements have demonstrated that trapping times, although different for holes and electrons, are typically in the order of tens or hundreds of ps, [74] a timescale much longer than the one investigated in our measurements. Therefore, it is reasonable to conclude that, although present, trap states should not significantly contribute to the recorded PC-2DES response.

All this discussion confirms that our samples are characterized by very complex electronic structures where different phenomena and size inhomogeneity make the PC-2DES interpretation very challenging. Theoretical simulations in collaboration with Prof. Francoise Remacle (University of Liège) are currently underway to try to untangle such a complex problem.

---

[6] Kindly provided by the group of Prof. Francoise Remacle (University of Liège).

Meanwhile, an important observation about our data is that, together with diagonal peaks, cross peaks are clearly observed as well. In order to investigate the origin of these cross-peaks it is necessary to study how they evolve with the population time. In Figure 5.6 we report the time evolution at relevant coordinates. The signal extracted at the positions pinpointed by each colored circle is shown in the four right panels as a function of the population time. A clear decay for all the relevant peaks is observed. A deeper analysis of the decay dynamics is reported in the next section, where we describe the results of the analysis performed with the global exponential fitting model previously introduced in Chapter 4, Section 4.8.
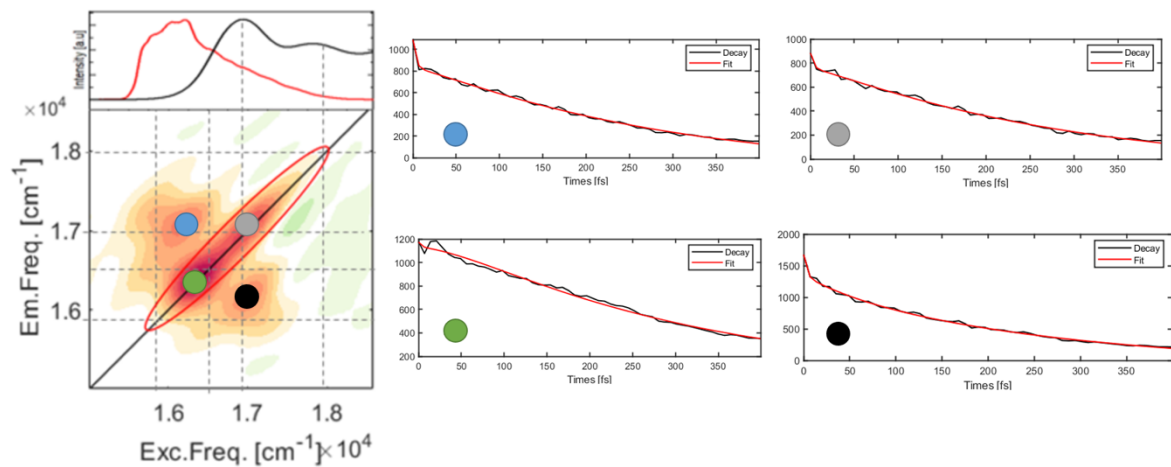
Figure 5.6: *Signal decay at relevant peaks coordinates over time. The four panels on the right illustrate the decay associated with the four peaks pinpointed by colored circles in the map. The black lines represent the experimental data, while the red curves are the fittings obtained with the global multi-exponential model.*

5.3 Global fitting analysis

In Chapter 4, Section 4.8, we observed that the 3D matrix of data can be conveniently analyzed by a *multi-exponential global fitting model*, which makes use of the fitting function defined in Equation 4.13 to simultaneously fit the signal decay at each coordinate of the 2DES maps.
The best fit was achieved by performing a global fit with four exponential decays having time constants of: 5 fs, 60 fs, 280 fs and >1ps. The last component is associated with relaxation dynamics that are developed in time scales much longer than the experimental time window investigated in our measurements and, therefore, will not be discussed here.
Figure 5.7 presents the DAS associated with the first three time components; below each DAS, we report a plot showing diagonal slices of the signal at relevant values of population times.
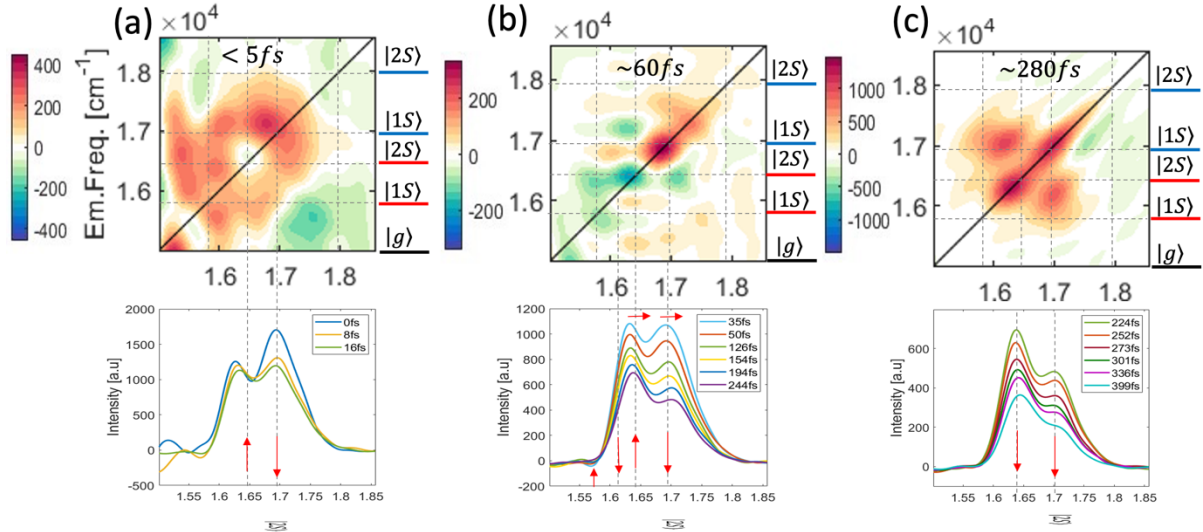
Figure 5.7*: In the upper panel, DAS maps associated to the three different time constants found according to the fitting model. In the lower panel, the cross section of the diagonal for different evolution times relevant to the time constant found by the global fitting.*

The first time constant (Figure 5.7a) describes an ultrafast decay (<5 fs) of all the peaks that appear in the 2DES maps. This kinetics develops in a timescale comparable with the pulse duration. In coherence-based 2DES, kinetic components characterized by time constants comparable with the pulse duration are usually discarded as they can be mainly attributed to interference and scattering phenomena known as "coherent artifacts" [75,76]. Nonetheless, in our case, the measured signal is not a coherent electric field but an incoherent photocurrent, which should not be affected by these phenomena. However, it has been demonstrated that when all four exciting pulses are overlapped in time on the sample, higher-order phenomena are likely to occur [77]. In our case, looking at the diagonal slices in the lower panel of Figure 5.7a, it is clear that this ultrashort time constant contributes more significantly to the decay of the upper diagonal peak than to the lower one.

The second dynamic process (Figure 5.7b) has a time constant of ~60 fs and shows a DAS map with several diagonal and cross peaks with different colors. As explained in Chapter 4, Section 4.8, a red (positive) peak in the DAS corresponds to a decay, whereas a blue/green (negative) peak implies a rise of the overall signal in the 2D maps. In the DAS of Figure 5.7b, there is a negative peak with coordinates corresponding to the lower diagonal peak at about 16200 cm^{-1}. On the contrary, a strong positive peak is recorded at diagonal coordinates corresponding to the upper diagonal peak at about 17000 cm^{-1}. This means that the intensity of the upper (lower) diagonal signal is decreasing (increasing) with a time constant of 60 fs. This is clearly visible also by inspecting the diagonal slices in the lower panel, where the increase of the signal at

lower frequency values causes an apparent blue shift of the main features. The interpretation of the physical process giving rise to this signal evolution is still under investigation. The similarity with previous results [78] seems to suggest that this process might be related to a localization of the excitation on the red states. According to this interpretation, it can likely be hypothesized that the photoexcitation prepares the system in a coherent superposition of states delocalized over more than one QD. Then, with a time constant of about 60 fs, this coherent superposition localizes on the lowest 'red' energy states. Decoherence processes with time constants in the order of a few tens of fs were already measured in QDs' solid-state assemblies by coherent-detected 2DES [51]. What is different (and very exciting) here is that these decoherence phenomena seem to contribute to the photocurrent signal. In other words, the functionality of a real device, measured as a generated photocurrent, is affected by coherent phenomena. If proven true, this discovery opens up a new avenue for the possible exploitation of quantum coherence in real devices. Additional measurements, also complemented by theoretical simulations, will be necessary to definitively prove this hypothesis.

Finally, the third dynamic process (Figure 5.7 c) has a time constant of 280 fs and corresponds to a uniform decay of all the peaks.

We also tried to verify the presence of beating components. However, the global fitting procedure could not identify any main oscillating contributions to the signal. However, it is known that this kind of analysis, because of its 'global' character, can capture only beating components significantly affecting the signal at several coordinates. Additional 'local' analyses at specific coordinates must be performed to ascertain with better precision the possible presence of weak oscillations.

Conclusions

This thesis is framed within the relatively unexplored landscape of action-based approaches to electronic bidimensional spectroscopy. The primary purpose of this study was, in fact, to try to contribute to the still limited yet rapidly growing literature on this topic.

In the first part of this work (Chapters 1-3), we built upon the formalisms and the theoretical notions at the base of the description of nonlinear optical responses and then proceeded to compare the action-based approach with the coherence-based one. The aim was to underline the main differences between these two approaches and specifically highlight the advantages of the action-based techniques. As starting samples, we choose materials based on semiconductor QDs, well-known for their unique optical and electronic properties mainly originating from quantum effects. Their ultrafast dynamics were already characterized in our group by coherence-based 2DES experiments, which revealed interesting quantum coherence phenomena and other processes taking place in ultrafast timescales. These properties also made them promising candidates to be studied with the new photocurrent-detected technique.

Differently from the coherence-based approach, the photocurrent-detected configuration requires samples with stringent characteristics (the photoactive units must be assembled on a conductive substrate to measure a photocurrent signal reliably). To this aim, an optoelectronic device based on CdSe QDs was specifically designed and prepared.

In the second part of this work (Chapters 4-5), we described the experimental solutions we employed in order to perform the experiment, from the configuration of the optical set-up and the phase-modulated detection of the signal to the processing and analysis methodologies exploited to extract the data.

As expected, the interpretation of the results in the action-based approach was not obvious and posed many challenges, especially given the fact that only a few literature works are available on the topic. Despite these difficulties, we managed to fulfill the goal of our initial project by demonstrating the potential of this recently proposed technique. In addition, according to a careful analysis of the results, we were able to propose a hypothesis on the possible link

between the presence of coherent phenomena and how they affect the functionality of a quantum-based device. If proven true, this discovery would open up a new avenue for the possible exploitation of quantum coherence in real operating devices.

In conclusion, this thesis not only contributes to the expanding field of ultrafast spectroscopy by addressing the existing research gap on action-based approaches but also demonstrates the potential associated with this innovative technique, paving the way for new perspectives in the field of 2DES. In addition, the experimental findings achieved in this work, despite their still preliminary nature, could also contribute to the expanding field of quantum nanoscience, providing insights for future investigations regarding the design and manipulation of QDs for applications in quantum technologies.

Bibliography

1. Brańczyk, A.M.; Turner, D. B.; Scholes, G. D. Crossing Disciplines - A View on Two-Dimensional Optical Spectroscopy. *Ann Phys* **2014**, 526(1–2): 31.

2. Gelzinis, A.; Augulis, R.; Butkus, V.; Robert, B.; Valkunas, L. Two-Dimensional Spectroscopy for Non-Specialists. *Biochimica et Biophysica Acta (BBA) - Bioenergetics* **2019**, 1860(4): 271.

3. Jonas, D.M. Two-Dimensional Femtosecond Spectroscopy. *Annu Rev Phys Chem* **2003**; 54(1): 425.

4. Collini, E. 2D Electronic Spectroscopic Techniques for Quantum Technology Applications. *The Journal of Physical Chemistry C.* **2021**; 125(24): 13096.

5. Bakulin, A.A.; Silva, C.; Vella, E.; Ultrafast Spectroscopy with Photocurrent Detection: Watching Excitonic Optoelectronic Systems at Work. *Journal of Physical Chemistry Letters*. **2016**; 7: 250.

6. Mukamel, S. *Principles of Nonlinear Optical Spectroscopy*; Oxford University Press, Ed.; **1995**.

7. Tokmakoff, A. *Nonlinear and Two-Dimensional Spectroscopy*; **2014**; online textbook.

8. Karki, K. J.; Widom, J. R.; Seibt, J.; Moody, I.; Lonergan, M. C.; Pullerits, T.; Marcus, A. H. Coherent Two-Dimensional Photocurrent Spectroscopy in a PbS Quantum Dot Photocell. *Nature Communications.* **2014**; 5: 5869.

9. Bolzonello, L.; Bernal-Texca, F.; Gerling, L.G.; Ockova, J.; Collini, E.; Martorell, J. et al. Photocurrent-Detected 2D Electronic Spectroscopy Reveals Ultrafast Hole Transfer in Operating PM6/Y6 Organic Solar Cells. *Journal of Physical Chemistry Letters*. **2021**; 12(16): 3983.

10. Röding, S. *Coherent Multidimensional Spectroscopy in Molecular Beams and Liquids Using Incoherent Observables Dissertation.* Universität Würzburg, **2017**.

11. Parson, W.W. *Modern Optical Spectroscopy*; Springer Berlin Heidelberg: Berlin, Heidelberg, **2015**.

12. Cho, M. Coherent Two-Dimensional Optical Spectroscopy. *Chemical Reviews.* **2008**; 108(4): 1331.

13. Kraack, J.P.; Buckup, T. Introduction to State-of-the-Art Multidimensional Time-Resolved Spectroscopy Methods. Vol. 376, Topics in Current Chemistry. Springer International Publishing; **2018**.

14. Tan, H.S., Theory and Phase-cycling Scheme Selection Principles of Collinear Phase Coherent Multi-dimensional Optical Spectroscopy, *Journal of Chemical Phys*ics. **2008**; 129(12): 124501.

15. Malý, P.; Lüttig, J.; Mueller, S.; Schreck, M.H.; Lambert, C.; Brixner, T. Coherently and Fluorescence-detected Two-dimensional Electronic Spectroscopy: Direct Comparison on Squaraine Dimers. *Physical Chemistry Chemical Physics*. **2020**; 22(37): 21222.

16. Kühn, O.; Mančal, T.; Pullerits, T. Interpreting Fluorescence Detected Two-Dimensional Electronic Spectroscopy. *Journal of Physical Chemistry Letters. American Chemical Society*. **2020**; 11(13): 838.

17. Nardin, G.; Autry, T.M.; Silverman, K.L.; Cundiff, S.T. Multidimensional Coherent Photocurrent Spectroscopy of a Semiconductor Nanostructure. *Optics Express*. **2013**; 21(23): 28617.

18. Tekavec, P.F.; Lott, G.A.; Marcus, A.H. Fluorescence-detected Two-dimensional Electronic Coherence Spectroscopy by Acousto-optic Phase Modulation. *Journal of Chemical Physics*. **2007**; 127(21): 214307.

19. Damtie, F.A.; Wacker, A.; Pullerits, T.; Karki, K.J. Two-dimensional Action Spectroscopy of Excitonic Systems: Explicit Simulation Using a Phase-modulation Technique. *Physical Review A*. **2017**; 96(5): 53830

20. Bruschi, M.; Gallina, F.; Fresch, B. Simulating Action-2D electronic Spectroscopy of Quantum Dots: Insights on the Exciton and Biexciton Interplay from Detection-mode and Time-gating. *Physical Chemistry Chemical Physics*. **2022**; 24(45): 27645.

21. Claussen, J.C.; Hildebrandt, N.; Susumu, K.; Ancona, M.G.; Medintz, I.L. Complex Logic Functions Implemented with Quantum Dot Bionanophotonic Circuits. *ACS applied materials & interfaces*. **2014**; 6(6): 3771.

22. Kairdolf, B.A.; Smith, A.M.; Stokes, T.H.; Wang, M.D.; Young, A.N.; Nie, S. Semiconductor quantum dots for bioimaging and biodiagnostic applications. *Annual Review of Analytical Chemistry*. **2013**; 6(1): 143.

23. Bera, D.; Qian, L.; Tseng, T.K.; Holloway, P.H. Quantum dots and their multimodal applications: A review. *Materials (Basel)*. **2010**; 3(4): 2260.

24. Cotta, M. A. Quantum Dots and their Applications: What Lies Ahead? *ACS Applied Nano Materiarls.* **2020**, 3(6), 4920.

25. Norris, D.J.; Bawendi, M.G. Measurement and assignment of the size-dependent optical spectrum in CdSe quantum dots. *Physical Review B*. **1996**; 53(24): 16338.

26. Kamat, P. V.; Scholes, G.D. Quantum Dots Continue to Shine Brightly. *Journal of Physical Chemistry Letters. American Chemical Society*. **2016**; 7: 584.

27. Kittel, C. *Introduction to Solid State Physics*. 8th ed., John Wiley & Sons, **2004**.

28. Mohan Bhagyaraj, S.; Oluwafemi, O. S.; Kalarikkal, N.; Thomas, S. *Synthesis of Inorganic Nanomaterials.* Elsevier: Amsterdam, NL, **2018**.

29. Davydov, A. S. *Theory of Molecular Excitons*. 1st ed.; Plenum Press: New York, NY, USA, **1971**.

30. Scholes, G. D.; Rumbles, G. Excitons in Nanoscale Systems. *Nature Materials.* **2006**; 5(9): 683.

31. Dramićanin, M. *Luminescence Thermometry*. Elsevier: Amsterdam, NL, **2018**.

32. Efros, A. Interband light absorption in semiconductor spheres. *Soviet Physics. Semiconductors.* **1982**; 16(7): 772.

33. Fu, H.; Wang,L.W.; Zunger,A. Excitonic Exchange Splitting in Bulk Semiconductors. *Physical Review B.* **1999**; 59(8): 5568.

34. Gao, Y.; Yin, P. Synthesis of Cubic CdSe Nanocrystals and theirs Spectral Properties. *Nanomaterials and Nanotechnology.* **2017**; 7: 1.

35. Mushonga, P.; Onani, M.O.; Madiehe, A.M.; Meyer, M. Indiumphosphide-based Semiconductor Nanocrystals and their Applications. *Journal of Nanomaterials* **2012**; 2012:1.

36. Klimov, V.I. *Nanocrystal Quantum Dots*, 2nd ed.; CRC Press: Boca Raton, FL, USA, **2017**.

37. Gaponenko, S.V. *Optical Properties of Semiconductor Nanocrystals*; Cambridge University Press: Cambridge, UK, **1998**.

38. Donegá de Mello, C. Synthesis and Properties of Colloidal Heteronanocrystals. *Chemical Society Reviews.* **2011**; 40:1512.

39. Konstantatos, G.; Sargent, E.H. *Colloidal Quantum Dot Optoelectronics and Photovoltaics*. Cambridge University Press: Cambridge, UK, **2013**.

40. Willatzen, M.; Lew Yan Voon, L. *The k·p Method: Electronic Properties of Semiconductors*. Springer: Berlin, DE, **2009**.

41. Luttinger, J.M.; Kohn, W. Motion of Electrons and Holes in Perturbed Periodic Fields. *Physical Reviews.* 1955; *97*: 869.

42. Kane, E.O. Band Structure of Indium Antimonide. *Journal of Physical Chemistry. Solids.* **1957**; 1(4): 249.

43. Ekimov, A.I.; Hache, F.; Schanne-Klein, M.C.; Ricard, D.; Flytzanis, C.; Kudryavtsev, I.A.; Yazeva, T.V.; Rodina, A.V.; Efros, A.L. Absorption and Intensity-dependent Photoluminescence Measurements on CdSe Quantum Dots: assignment of the First Electronic Transitions. *Journal of the Optical Society of America B.* **1993**, 10(1): 100.

44. Collini, E.; Gattuso, H.; Levine, R.D.; Remacle, F. Ultrafast Femtoseconds Coherent Excitonic Dynamics in CdSe Quantum Dots Assemblies Addressed and Probed by 2D Electronic Spectroscopy. *Journal of Chemical Physics.* **2021**; 154(1): 14301.

45. Collini, E.; Gattuso, H.; Kolodny, Y.; Bolzonello, L.; Volpato, A.; Fridman, H. T.; Yochelis, S.; Mor, M.; Dehnel, J.; Lifshitz, E.; Paltiel, Y.; Levine, R.D.; Remacle, F. Room-temperature Inter-dot Coherent Dynamics in Multilayer Quantum Dot Materials. *Journal of Physical Chemistry C.* **2020**; 124(29):16222.

46. Yu, Z.; Li, J.; O'Connor, D.B.; Wang, L.W.; Barbara, P.F. The Influence of Electron-hole Interaction of Colloidal CdS Quantum Dots on the Value of the Resonant Stokes Shift. *Journal of Physical Chemistry B.* **2003**; 107: 5670.

47. Brus, L.E. Electronic Wave Functions in Semiconductor Clusters: Experiment and Theory. *Journal of Physical Chemistry.* **1986**; 90: 2555.

48. Brus, L.E. Electron-electron and Electron-hole Interactions in Small Semiconductor Crystallites: The Size Dependence of the Lowest Excited Electronic State. *The Journal of Chemical Physics.* **1984**; 80(9): 4403.

49. Brus, L.E. A Simple Model for the Ionization Potential, Electron Affinity, and Aqueous Redox Potentials of Small Semiconductor Crystallites. *The Journal of Chemical Physics.* **1983**; 79(11): 5566.

50. Koley, S.; Cui, J.; Panfil, Y.E.; Banin, U. Coupled Colloidal Quantum Dot Molecules. *Accounts of Chemical Research.* **2021**; 54(5), 1178.

51. Collini, E.; Gattuso, H.; Bolzonello, L.; Casotto, A.; Volpato, A.; Dibenedetto, C.N.; Fanizza, E.; Striccoli, M.; Remacle, F. Quantum Phenomena in Nanomaterials: Coherent Superpositions of Fine Structure States in CdSe Nanocrystals at Room Temperature. *Journal of Physical Chemistry C.* **2019**; 123 (51), 31286.

52. Komarova, K.; Gattuso, H.; Levine, R.D.; Remacle, F. Quantum Device Emulates the Dynamics of Two Coupled Oscillators. *Journal of Physical Chemistry Letters*. **2020**; 11(17): 6990.

53. Dibenedetto, C.N.; Fanizza, E.; Brescia, R. et al. Coupling Effects in QD Dimers at Sub-nanometer Interparticle Distance. *Nano Research*. **2020**; 13: 1071.

54. Dibenedetto, C.N.; Fanizza, E.; de Caro, L.; Brescia, R.; Panniello, A.; Tommasi, R. et al. Coupling in Quantum Dot Molecular Hetero-assemblies. *Materials Research Bulletin.* **2022**; 111578:146.

55. Tekavec, P.F.; Myers, J.A.; Lewis, K.L.M.; Fuller, F.D.; Ogilvie, J.P. Effects of Chirp on Two- Dimensional Fourier Transform Electronic Spectra. *Optics Express*. **2010**; 18 (11): 11015.

56. Fuller, F.D.; Ogilvie, J.P. Experimental Implementations of Two-Dimensional Fourier Transform Electronic Spectroscopy. *Annual Reviews of Physical Chemistry.* **2015**; 66 (1): 667.

57. Volpato, A. *Innovative Strategies in Coherent Multidimensional Electronic Spectroscopy*. Ph.D. Thesis, University of Padova, **2017**.

58. Wollenhaupt, M.; Assion, A.; Baumert, T. Springer Handbook of Lasers and Optics. New York: Springer Science + Business Media, **2007**.

59. Fastlite, "Dazzler System Operating Manual", Tech. rep., Fastlite (**2005**).

60. Tournois, P. Acousto-optic Programmable Dispersive Filter for Adaptive Compensation of Group Delay Time Dispersion in Laser Systems. *Optics Communications.* **1997**; 140(4-6): 245.

61. Draeger, S.; Röding, S.; Brixner, T. Rapid-Scan Coherent 2D Fluorescence Spectroscopy. *Optics Express*. **2017**, 25 (4), 3259.

62. Fleming, G.R. *Chemical Applications of Ultrafast Spectroscopy,* New York: Oxford Univ. Press. **1986**.

63. Li, H.; Bristow, A.D.; Siemens, M.E.; Moody, G.; Cundiff, S.T. Unraveling Quantum Pathways Using Optical 3D Fourier-Transform Spectroscopy. *Nature Communications.* **2013**, 4(1), 1390.

64. Cundiff, S.T. Optical Three Dimensional Coherent Spectroscopy. *Physical Chemistry Chemical Physics.* **2014**, 16(18), 8193.

65. Mullen, K.M.; van Stokkum, I.H.M. The Variable Projection Algorithm in Time-Resolved Spectroscopy, Microscopy and Mass Spectrometry Applications. *Numerical Algorithms.* **2009**, 51(3), 319.

66. Camargo, F.V.A.; Anderson, H.L.; Meech, S.R.; Heisler, I.A. Time-Resolved Twisting Dynamics in a Porphyrin Dimer Characterized by Two-Dimensional Electronic Spectroscopy. *Journal of Physical Chemistry B*. **2015**, 119(46), 14660.

67. Volpato, A.; Bolzonello, L.; Meneghin, E.; Collini, E. Global Analysis of Coherence and Population Dynamics in 2D Electronic Spectroscopy. *Optics Express*. **2016**, 24(21), 24773.

68. Malý, P.; Lüttig, J.; Mueller, S.; Schreck, M.H.; Lambert, C.; Brixner, T. Coherently and Fluorescence-detected Two-dimensional Electronic Spectroscopy: Direct Comparison on Squaraine Dimers. *Physical Chemistry Chemical Physics*. **2020**; 22(37): 21222.

69. Read, E.L.; Engel, G.S.; Calhoun, T.R.; Mančal, T.; Ahn, T.K.; Blankenship, R.E.; Fleming, G.R. Cross-Peak-Specific Two-Dimensional Electronic Spectroscopy. *Proceedings of the National Academy of Sciences*. **2007**; 104(36): 14203.

70. Hamm, P.; Zanni, M.T. *Concepts and Methods of 2D Infrared Spectroscopy*. Cambridge University Press. **2011**.

71. Pein, B.C.; Lee, C.K.; Shi, L.; Shi, J.J.; Chang, W.; Hwang, H.Y.; Scherer, J., Coropceanu, I.; Zhao, X.; Zhang, X.; Bulović, V.; Bawendi, M.G.; Willard, A.P.; Nelson, K.A. Terahertz-Driven Stark Spectroscopy of CdSe and CdSe-CdS Core-Shell Quantum Dots. *Nano Letters*, **2019**; 19(11): 8125

72. Empedocles, S.A.; Bawendi, M.G.; Quantum-Confined Stark Effect in Single CdSe Nanocrystallite Quantum Dots. *Science.* **1997**; 278, 2114.

73. Houtepen, A.J.; Hens, Z.; Owen, J.S.; Infante, I. On the Origin of Surface Traps in Colloidal II–VI Semiconductor Nanocrystals. Chemical Materials. **2017**; 29: 752.

74. Brosseau, P.J.; Geuchies, J.J.; Jasrasaria, D.; Khambhapati, P. *et al.* Ultrafast Hole Relaxation Dynamics in Quantum Dots Revealed by Two-dimensional Electronic Spectroscopy. *Communication Physics*. **2023**; 6(1): 48.

75. Lebedev, M.V.; Misochko, O.V.; Dekorsy, T.; Georgiev, N. On the Nature of "Coherent Artifact." *Journal of Experimental and Theoretical Physics*. **2005**, 100(2), 272.

76. Ferwerda, H.A.; Terpstra, J.; Wiersma, D.A. Discussion of a '"Coherent Artifact"' in Four-wave Mixing Experiments. *Journal of Chemical Physics*. **1989**; 91(6): 3296.

77. Mueller, S.; Brixner, T. Molecular Coherent Three-Quantum Two-Dimensional Fluorescence Spectroscopy. *Journal of Physical Chemistry Letters.* **2020**; 11: 5139

78. Meneghin, E.; Volpato, A.; Cupellini, L.; Bolzonello, L.; Jurinovich, S.; Mascoli, V.; Carbonera, D.; Mennucci, B.; Collini, E. Coherence in Carotenoid-to-chlorophyll Energy Transfer. *Nature Communications*. 2018; 9(1): 3160.